Constraining the Reaction Rate of Criegee Intermediates with Carboxylic Acids during the Multiphase Ozonolysis of Aerosolized Alkenes

Ryan Reynolds,[1,2] Musahid Ahmed[1] and Kevin R. Wilson[1*]

[1]*Chemical Sciences Division, Lawrence Berkeley National Laboratory, Berkeley, CA, 94720, USA*

[2]*Department of Chemistry, University of California, Berkeley, CA 94720, USA*

Abstract

Criegee intermediates (CI) are central to the ozonolysis of unsaturated organic compounds, controlling the formation of small fragmentation reaction products and higher molecular weight oligomeric compounds through competing unimolecular and bimolecular pathways. In particular, the reaction of thermalized CI with carboxylic acids (RCOOH) to produce oligomeric α-acyloxyalkyl hydroperoxides (AAHPs) is of interest to the chemical transformation of organic compounds in the atmosphere. In the gas phase, the CI + RCOOH reaction proceeds at super-collisional rates, consistent with a barrierless reaction mechanism. However, the rate of this reaction in condensed phases remains uncertain. Here we report the results of aerosol flow tube studies of the ozonolysis of submicron organic aerosol containing mixtures of an internal *n*-alkene (Z-9-tricosene, Tri) and a saturated acid (2-hexyldecanoic acid, HDA). The decay of the reactants and formation of reaction products are monitored using Atmospheric Pressure Chemical Ionization mass spectrometry (APCI-MS). A sixfold-decrease in the reactive uptake of ozone is observed with increasing acid concentration, consistent with a previous study using alcohol additives. The decay of HDA with ozone exposure shows that HDA scavenges CI at rates comparable to competing unimolecular pathways involving CI. The decay kinetics of HDA are analyzed using a simple kinetic model in order to constrain the ratio of the CI + RCOOH and unimolecular CI rate constants. Empirical fitting to this model, combined with theoretical estimates of the unimolecular loss rate, yields a CI + RCOOH rate constant of $1.85 \pm 0.27 \times 10^{-19}$ cm^3 $molec^{-1}$ s^{-1}, which is six orders of magnitude slower than the expected diffusion limit in a liquid organic matrix. Stochastic kinetic simulations are conducted with different values of the CI + RCOOH rate constant to validate this result, and show that the diffusion limited rate is indeed much too rapid to reproduce the experimental results.

* Correspondence to: krwilson@lbl.gov

Keywords: APCI mass spectrometry, chemical kinetics, organic aerosol, lipids, organic hydroperoxides, oligomers, radical oxidation

1. Introduction

Criegee Intermediates (carbonyl oxides), formed during the ozonolysis of unsaturated organic compounds (Scheme 1), are crucially important oxidants due to their high reactivity and diverse reaction pathways.[1] Extensive gas-phase studies have been conducted on these short-lived intermediates to understand their chemistry, which has been enabled by direct detection of these species in recent years.[2,3] The reaction between a Criegee Intermediate and an organic acid is observed to occur near or exceeding the calculated hard-sphere collision limit in direct measurements.[4,5] As a result, this reaction pathway is thought to represent a significant sink of Criegee Intermediates in the atmosphere. Additionally, the oligomeric hydroperoxide products of this reaction are thought to contribute to atmospheric particle formation.[4]

In condensed phases where both unsaturated organics and saturated carboxylic acids (RCOOH) are present, the loss of RCOOH[6] and subsequent formation of α-acyloxyalkyl hydroperoxides (AAHPs)[7] has been observed during ozonolysis. With analogy to the gas phase mechanism, this reaction is attributed to Criegee Intermediates in the organic matrix which have been stabilized by thermalizing collisions. (These stabilized Criegee Intermediates will furthermore be referred to simply as CI.) The CI + RCOOH reaction is significant to the ozonolysis of aerosol composed of unsaturated fatty acids, such as oleic acid, where peroxidic products are estimated to account for between 30–68% of the product yield.[8,9] However, the kinetics of this CI consumption channel are underdetermined in the condensed phase, which has resulted in significant uncertainty in models of heterogeneous ozonolysis in organic aerosol, where rate constants for the CI + RCOOH reaction vary over six orders of magnitude.[10,11] Thus, measurements of this rate coefficient would improve the prediction of reaction kinetics and product distributions in models of heterogeneous chemistry.

In this study, a flow tube reactor is used to investigate the heterogeneous ozonolysis of aerosols of a mixture of a model alkene, cis-9-tricosene (**Tri**, $C_{23}H_{46}$ — MW 322), and a saturated organic acid, 2-hexyldecanoic acid (**HDA**, $C_{16}H_{32}O_2$ — MW 256). This mixture is used to constrain the rate of reaction between particle-bound CI and organic acid functional groups. Tri is a suitable model alkene for this purpose as it contains a single double bond, is a liquid at room temperature, and contains no oxygenated functional groups. The aldehydes produced from ozonolysis of Tri (Scheme 1A) are volatile and largely partition out of the aerosol during reaction, thus restricting the number of secondary reaction channels available to the CI.[12,13] Additionally, the decay rate of Tri during ozonolysis is highly sensitive to additives that behave as CI scavengers, as a result of radical chain oxidation chemistry.[12] HDA is a suitable model for fatty acid functionality (RCOOH), as its saturated chain is unreactive to both O_3 and CI, thereby restricting its chemical reactivity to its acid head group. By measuring the decay kinetics of both Tri and HDA upon exposure to ozone, the production rate of CI, the consumption of CI by a condensed-phase organic acid, and the interaction between the CI + RCOOH and radical chain cycling reactions are probed simultaneously. A simple kinetic model is used to analyze these observations and shows that the kinetic observations can be explained by the competition between bimolecular and unimolecular sinks for CI, allowing for estimation of the CI + RCOOH rate constant. This result is validated using explicit kinetic simulations, which incorporate a detailed mechanism derived from previous work.[12]

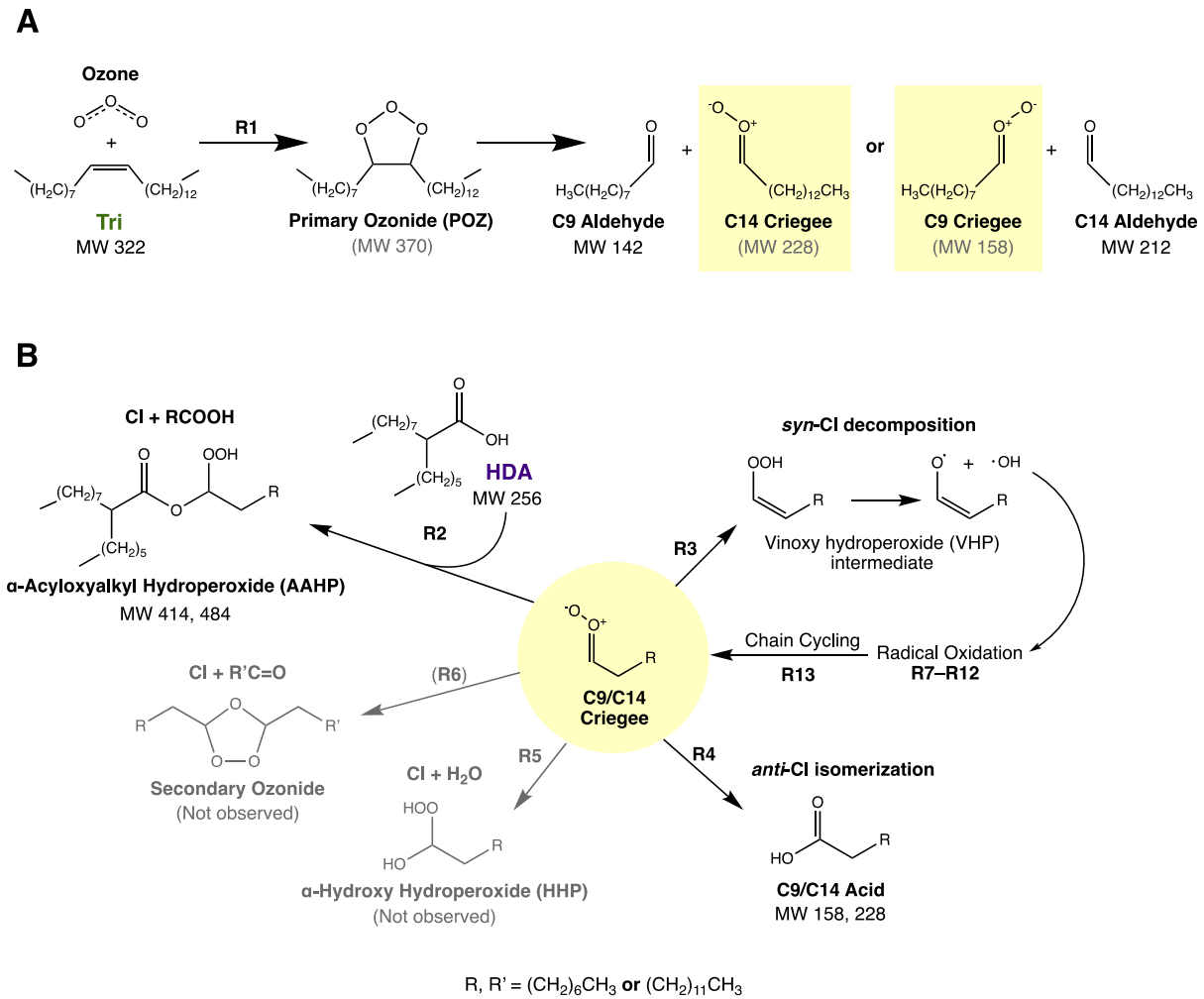

Scheme 1: Mechanism of ozonolysis and secondary chemistry observed in this system, as well as the identities of major reactants, products, and intermediates. (**a**) The primary ozonolysis reaction (R1), displaying the reactants (Tri, ozone), the primary ozonide (POZ) intermediate, and the two possible pairs of reaction products. The POZ is assumed to rapidly decompose, and CI are not observed directly. (**b**) The secondary chemistry, consisting of reaction of CI (center) with HDA (R2), as well as additional unimolecular (R3, R4) and bimolecular (R5, R6) sinks of CI considered in this study. Secondary ozonide and HHP products are not observed. Refer to Table S2 (Supplementary Information) for a complete mechanism description, including the radical oxidation (R7-R12) and chain cycling (R13) steps included in stochastic kinetic simulations.

2. Experimental

2.1. Experimental Description

A flow tube reactor (Fig. S1) is used to measure the ozonolysis of Tri:HDA mixtures in mole ratios of 100:0, 95:5, 80:20, 60:40, 40:60, and 15:85 (see Table S1 for a detailed list of experimental

conditions). Particles are generated by homogeneous nucleation in a tube furnace. For each mixture, a Pyrex tube is charged with small amounts of Tri (97%, Sigma-Aldrich Co.) and HDA (96%, Sigma-Aldrich Co.), between 2–4 mL in total, using a micropipette. The tube is inserted into the furnace and heated to 110–115 ˚C. 0.3 standard liters per minute (SLM) of dry nitrogen at room temperature is passed through the Pyrex tube, producing polydisperse particles. As the vapor pressures of both organics are expected to be similar (~$1x10^{-5}$ torr at 25 ˚C), the composition of the particles is assumed to match that of the bulk mixture. The resulting flow passes through an annular charcoal denuder to remove residual organics in the gas phase, and then enters the flow tube reactor. Particle distributions are measured at the exit of the flow tube using a Scanning Mobility Particle Spectrometer (SMPS) consisting of a Differential Mobility Analyzer (3080, TSI Inc.) and a Condensation Particle Counter (3025A, TSI Inc.) For pure Tri experiments, the mean diameter of the log-normal distribution lies between 430–480 nm with a geometric standard deviation (σ_g) of 1.29. The tail of this distribution extends beyond the measurement range of the SMPS, so this value for σ_g is an underestimate. In mixture experiments, the mean diameters of the particle distributions lie between 245–370 nm, with σ_g ranging from 1.35 to 1.68.

The cylindrical quartz flow tube reactor is 147 cm in length and 2.4 cm in diameter, resulting in a volume of 665 cm^3, which, given a typical total flow of 1.03 SLM, results in a residence time of approximately 39 seconds. In addition to the 0.3 SLM flow of particle-laden N_2, 0.5 SLM of pure N_2 and 0.2 SLM of dry O_2 (99.993%, Praxair) are introduced at the inlet of the reactor. During reactions, ozone is generated using a 0.1 SLM flow of O_2 into a corona discharge source (Ozone Services, Yanco Industries), after which this flow is diluted with 5 SLM of N_2 in a glass mixing cell. The concentration of O_3 in the flow is measured with a commercial ozone monitor (106M, 2B Technologies) at the exit of the mixing cell. The voltage on the corona

discharge source can be adjusted to achieve O_3 concentrations between 8–640 ppm. A rotameter (King Instruments) is used to deliver 30 standard cubic centimeters per minute (SCCM) of the diluted $O_3/O_2/N_2$ flow into the flow tube reactor, where resulting O_3 concentrations range from 0.2-20 ppm. At the exit of the flow tube, the flow passes through an annular denuder packed with Carulite 200 catalyst, which catalytically destroys O_3 and terminates the reaction. During the course of all experiments described here, no unexpected or unusually high safety hazards were encountered.

2.2. APCI Mass Spectrometry

The reaction kinetics are monitored using a Thermo Scientific Velos Pro LTQ Mass Spectrometer fitted with an Atmospheric Pressure Chemical Ionization (APCI) source, modified to take particle-laden gas-phase flow through a ceramic inner bore, as described by Roveretto and co-workers[14] and shown in Fig. S1. The outer ceramic inlet tube is heated to 180 ˚C to vaporize the aerosol particles prior to entering the ionization region. The flow into the inlet of the MS includes N_2 sheath gas at a flow setting on the mass spectrometer of 1.8 (arbitrary units). Auxiliary gas flow is not used. Mass spectra are recorded over the mass range of m/z = 50–1000, in both positive and negative ion mode. In positive ion mode, the corona discharge needle is set to 4 kV with a typical current of 5μA, while in negative ion mode the discharge voltage is set to 1.5kV with a typical current of 8μA. The analyzer region of the mass spectrometer is maintained with Helium gas (99.998%, Airgas) at 40 psi.

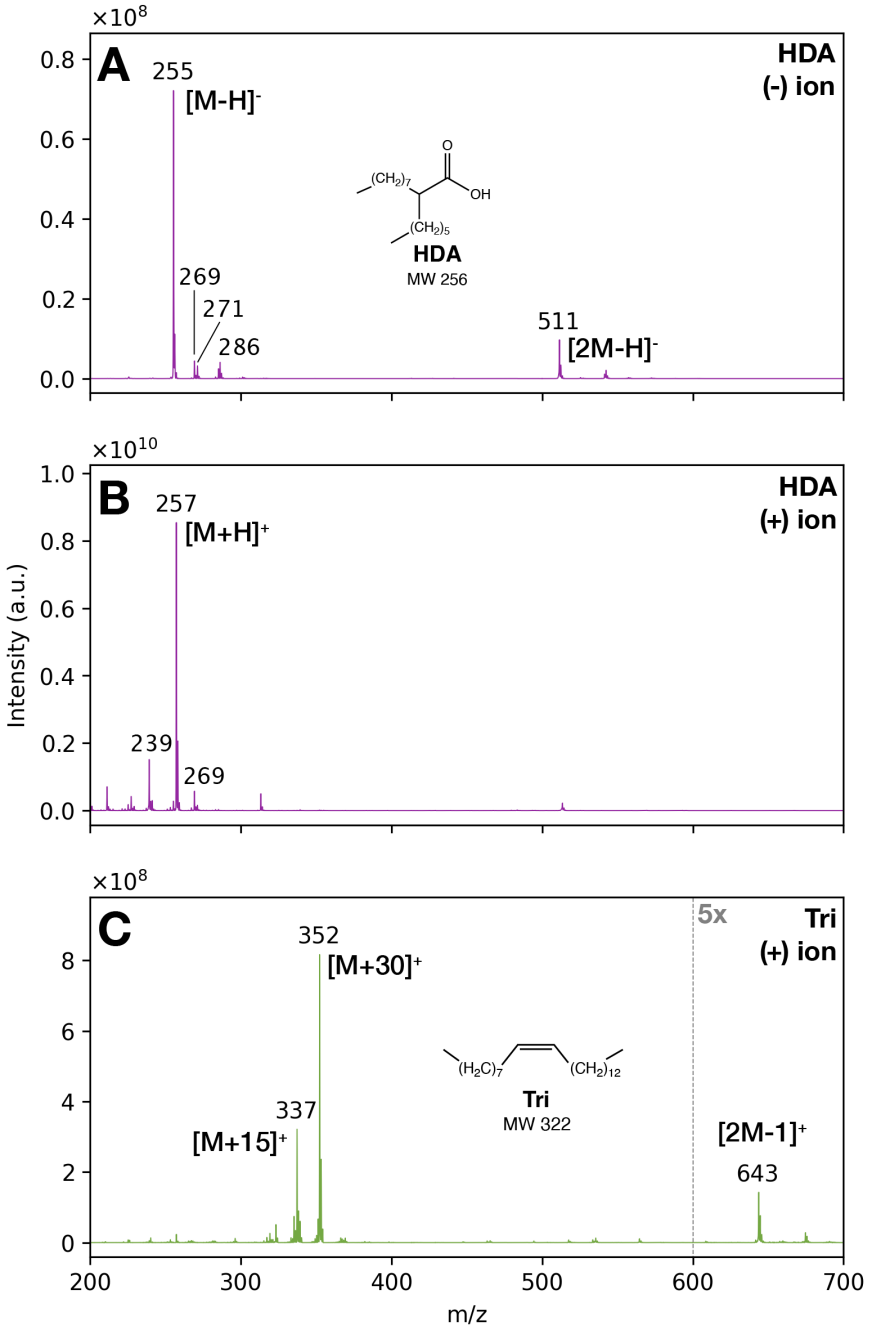

Figure 1: APCI Mass spectra of aerosols of pure reactants. a) HDA, negative ion mode mass spectrum, showing the deprotonated dimer peak at *m/z* = 511. b) HDA positive ion mode mass spectrum. c) Tri positive ion mode mass spectrum, with the region from *m/z* = 600 to 700 in the Tri spectrum magnified by a factor of 5 to highlight the $[2M-1]^+$ dimer peak at *m/z* = 643.

The negative and positive ion mass spectra of HDA, and the positive ion spectrum of Tri, are shown in Fig. 1A-C. The peak at *m/z* = 255 in Fig. 1A corresponds to the $[M-H]^-$ ion of HDA. Deprotonation of acidic functional groups is a dominant mechanism by which APCI produces negative ions.[15,16] The small clusters of peaks above *m/z* = 255 likely correspond to ketone or alcohol products of radical chemistry occurring in the ionization region, resulting in the +14 and +16 peaks visible in the clusters. Also shown in Fig. 1A is a strong peak at *m/z* = 511, corresponding to a $[2M-H]^-$ deprotonated dimer of HDA. In the positive ion mode, APCI primarily generates ions through protonation of oxygenated functional groups to form $[M+H]^+$ ions[16] resulting in the *m/z* = 257 peak observed in Fig. 1B, but peaks attributed to oxidation (*m/z* = 269), water loss (m/z = 239), and background species can also be observed. Note that the magnitude of the signal in the positive ion spectrum is two orders of magnitude larger than the negative ion spectrum for HDA.

Tri, being entirely aliphatic, undergoes a different mechanism for positive ion formation. As seen in Fig. 1C, the major positive ion is *m/z* = 352, corresponding to $[M+30]^+$, with a smaller peak at *m/z* = 337 (i.e., $[M+15]^+$). Aliphatic compounds in APCI sources typically undergo ionization through hydride charge transfer, which can be accompanied by reductive elimination of H_2, resulting in an $[M-3]^+$ fragment ion.[17] In the presence of ambient H_2O, this ion can then be hydrated to form an $[M+15]^+$ species, or in an excess of O_2 in the ionization region, addition of HO_2 appears to be favored, resulting in the formation of $[M+30]^+$. Dimer formation following hydride charge transfer forms the $[2M-1]^+$ ion visible at *m/z* = 643 in Fig. 1C. The negative-mode spectrum for Tri shows signs of similar charge-transfer and oxidation or hydration ionization mechanisms, however the signal from neat Tri in negative mode APCI is extremely small. As a result, the negative ion polarity was not used to quantify Tri decay kinetics and is not shown.

3. Results

3.1. Reaction Products: Mass Spectra

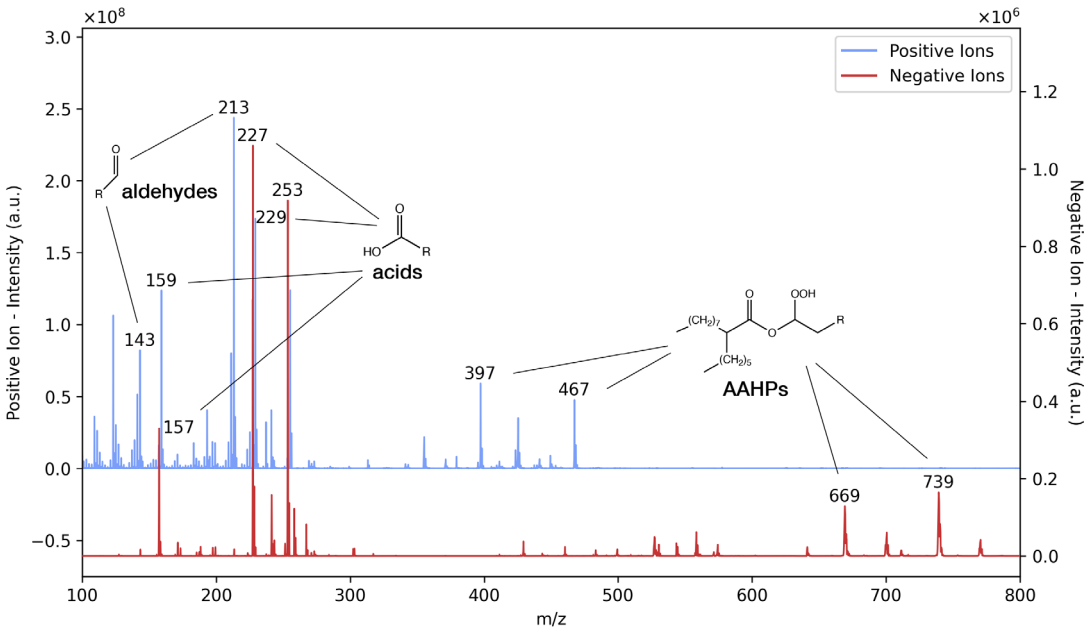

Figure 2: Representative difference mass spectra of an ozonized 80:20 Tri:HDA reaction mixture. The positive ion mode spectrum (blue, upper) and negative ion mode spectrum (red, lower) are presented offset on the same axes to show the complementary peaks in the lower molecular weight region of the spectrum. Major peaks of the AAHP products are clearly visible in both positive ion mode (*m/z* = 397, 467) and negative ion mode (*m/z* = 669, 739).

Upon exposure to ozone, the mass spectrum of the reaction matrix (Fig. 2) exhibits a decay in the intensity of reactant peaks and the growth of product peaks, corresponding to both lower-molecular weight products from ozonolysis and new higher-molecular weight AAHP products, consistent with the mechanism shown in Scheme 1. Upon accommodating to the surface of the aerosol particle, an ozone molecule encounters the carbon-carbon double bond of Tri and undergoes cycloaddition to form a primary ozonide (POZ), which rapidly decomposes into one of two pairs of carbonyl oxide/aldehyde coproducts (R1, Scheme 1A). The positive ion mode peaks at *m/z* 143 and 213 in Fig. 2 correspond to the $[M+H]^+$ ions of nonanal ($C_9H_{18}O$, MW = 142) and

tetradecanal ($C_{14}H_{28}O$, MW = 212). Since there are no labile hydrogens to be removed during chemical ionization, no corresponding negative ions are observed for the aldehydic products. The POZ ($C_{23}H_{46}O_3$, MW = 370) is not observed in either ionization mode.

After decomposition of the POZ, the chemistry in this reaction system, including radical chemistry, is mediated by CIs, with the four reactions most significant for this study highlighted in Scheme 1B. The dominant unimolecular reaction of the *syn* CI conformer, which has its terminal oxygen and alkyl chain on the same side of the C=O double bond, generates a hydroxyl radical *via* a vinyl hydroperoxide (VHP) intermediate formed through a 1,4 hydrogen shift (R3, Scheme 1B). The presence of this reactive channel in the Tri + O_3 system has been confirmed in a previous study[18] through the detection of ·OH radical oxidation products. Unfortunately, the products of this ·OH radical-initiated chemistry (R7-R12) (e.g., TriO, $TriO_2$, etc.) are isobaric with the oxidized background molecular ions observed in the APCI spectrum of neat Tri. Thus, products corresponding to radical chemistry cannot be definitively observed under current experimental conditions. The *anti* conformer of the CI, which has its terminal oxygen atom pointed away from the alkyl substituent, can isomerize, forming a carboxylic acid (R4, Scheme 1B) *via* 1,3-cyclization followed by a ring-opening rearrangement. The two corresponding acids in this reaction system (nonanoic acid – $C_9H_{18}O_2$, MW 158; and tetradecanoic acid – $C_{14}H_{28}O_2$, MW 228) are clearly observed as pairs of $[M+H]^+$ and $[M-H]^-$ ions in the overlapping positive and negative ion spectra, appearing at *m/z* = 157 and 159, and m/z = 227 and 229 in Fig. 2.

Either conformer of the CI can undergo bimolecular reactions to form hydroperoxide products, though with different rates.[2,19,20] Reaction of CI with water (R5, Scheme 1B) will lead to the formation of α-hydroxy hydroperoxides (HHP), which may potentially decompose into corresponding carbonyl species *via* loss of H_2O_2.[21] Finally, the reaction between CI and carboxylic

acids (R2, Scheme 1B) form α-acyloxyalkyl hydroperoxides (AAHP), containing an ester functional group. The primary AAHP products formed in this system are $C_{25}H_{48}O_4$ (MW = 414) and $C_{30}H_{58}O_4$ (MW = 484), resulting from the addition of either the 9- or 14-carbon CI to HDA. The two major high-molecular weight peaks in the positive ion spectrum, *m/z* = 397 and *m/z* = 467, are $[M-17]^+$ ions of these AAHPs, corresponding to OH loss. An identical pattern is visible in the negative ion spectrum, albeit at *m/z* 669 and 739. Collision-Induced Dissociation (CID) of these peaks (see Figs. S2 and S3) reveals them to be $[M+255]^-$ clusters, formed from the complex of the C_{25} and C_{30} AAHPs with an HDA carboxylate anion. Such clustering behavior is reasonable given the high ionization efficiency of negative mode APCI toward acids and the dimerization of HDA described earlier.

3.2. Reaction Kinetics: Uptake Coefficients

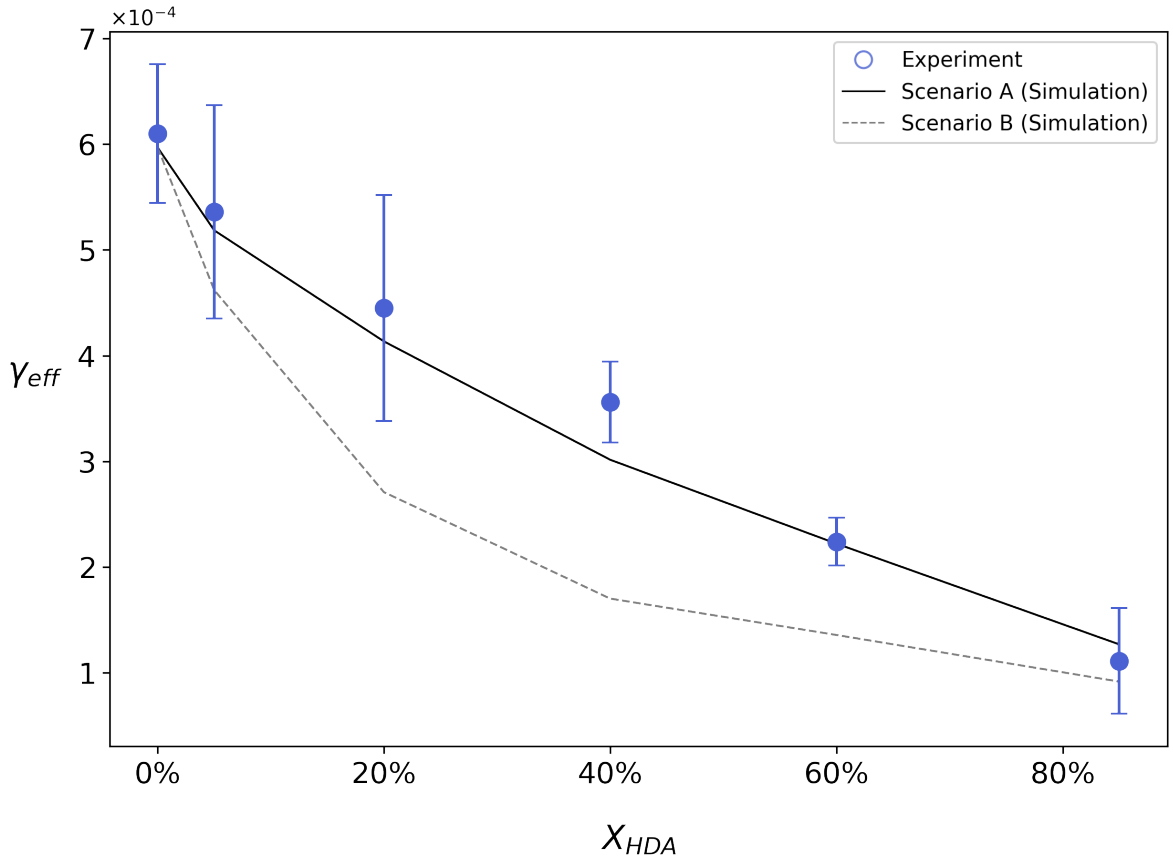

Figure 3: Reactive uptake coefficients as a function of HDA mole fraction. Points correspond to the mean of at least 3 experimental measurements, and error bars represent ±1 standard deviation from the mean. Lines represent the results of explicit kinetic simulations under two different modeling scenarios (see Section 4.3): Scenario A (solid black line), where k_{AAHP} is fixed at 2.1x10^{-19} cm^3 molec.$^{-1}$ sec.$^{-1}$ in accord with the empirical rate presented in Section 4.2; and Scenario B (dashed black line), where k_{AAHP} is fixed at 1x10^{-13} cm^3 molec.$^{-1}$ sec.$^{-1}$ to represent a rate limited only by diffusion in the organic matrix. Further model sensitivity tests of k_{AAHP} within an order of magnitude of the Scenario A value can be found in Fig. S10 of the Supporting Information.

The reaction probability of Tri, also termed the effective reactive uptake coefficient (γ_{eff}), is an informative metric of the rate of a heterogeneous reaction and has been defined previously.[22–24] Briefly, γ_{eff} here represents the ratio of the consumption rate of Tri (corrected for its mole fraction in the mixture) to the collision rate of gaseous ozone. Although γ_{eff} is generally less than 1, it can be > 1 in cases, such as in the presence of radical chain reactions, when the arrival of a molecule of the gaseous reactant results in the consumption of more than one molecule of the condensed

phase reactant.[22,24,25] In Fig. 3, γ_{eff} for Tri is observed to be a function of the mole fraction of HDA in the aerosol (X_{HDA}). γ_{eff} for neat Tri aerosol measured in this study is 6.5×10^{-4}, and is in agreement with previous measurements by Zeng and Wilson (5.2×10^{-4}, obtained using aerosol photoionization mass spectrometry).[12] Zeng notes that this condensed-phase γ_{eff} is an order of magnitude greater than a previous uptake coefficient obtained using the decay of gas phase ozone. This difference is attributed to radical chain cycling, which accounts for a significant amount of the Tri consumption during the reaction.[26] Similar to the behavior observed by Zeng *et al.* upon addition of a saturated alcohol, the uptake coefficient decreases with increasing mole fraction of HDA. For example, an aerosol composed of 40% HDA exhibits a twofold decrease in γ_{eff} relative to neat Tri. This suggests that presence of RCOOH behaves as a CI scavenger, as illustrated in Scheme 1B: instead of decomposing to form ·OH (R3), which accelerates Tri consumption through radical chain chemistry (R7–R13), CIs react preferentially with the acid functional group (R2) when HDA is present. Although Zeng did not report data for additive mole fractions greater than 40%, the trend appears to continue linearly: a mixture composed of 85% HDA yields a sixfold decrease in γ_{eff}. Following Zeng's previous work, the addition of CI to alkenes to form cyclic hydroperoxides is not thought to be kinetically significant in this system.[12] Furthermore, though HDA is expected to react with ·OH radicals, the rate of this reaction is expected to be an order of magnitude slower than that of ·OH addition to alkenes, which is the predominant radical initiation step in this mechanism.[27] Accordingly, assuming the sole reactive sinks for CI are isomerization to produce ·OH radical and bimolecular reaction with HDA, the decrease in uptake with increased HDA concentration suggests that the rates of these processes are competitive under the experimental conditions studied here. The decrease in γ_{eff} with [HDA] is accurately predicted by the kinetic model developed by Zeng *et al.*, which is slightly adapted to describe these experiments

as discussed in Section 4.3. The values of γ_{eff} predicted by the model for two values of the bimolecular rate coefficient k_{AAHP} are additionally shown in Fig. 3 as will be detailed below.

3.3. Reaction Kinetics: Decay of HDA

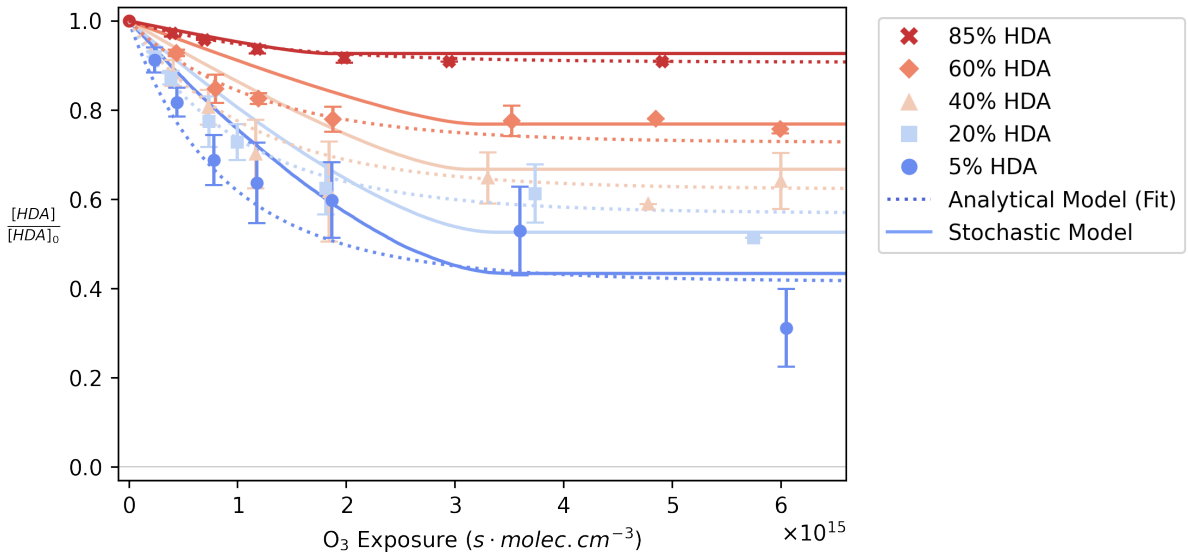

Figure 4: The decay of the HDA signal intensity with ozone exposure, normalized to unreacted HDA signal for aerosols having HDA mole fractions (from top to bottom) of 85%, 60%, 40%, 20%, and 5%. Symbols represent the mean of data from at least three experiments for each condition, and error bars represent ±1 standard deviation from the mean. Dotted lines represent fits of Eq. 6 to the experimental data, as described further in Section 4.2. Solid lines represent the results of explicit stochastic kinetic simulations under Scenario A, as described in Section 4.3.

The decay of HDA with increasing ozone exposure reveals additional information about the reactivity of CI in this matrix. In Fig. 4, the normalized intensity of the HDA signal is shown as a function of ozone exposure for each reaction mixture outlined in Table S1. In each experiment, the amount of HDA remaining approaches a limiting value that depends upon the initial HDA and Tri concentrations. For example, for an aerosol that is comprised of 85% HDA, nearly 90% of the HDA remains at the end of the reaction, while the mixture composed of only 5% HDA reaches a limiting value of roughly 30% after ozonolysis. As there are no other reactive sinks for HDA, this

decay in the HDA concentration arises from its reaction with CIs. It is apparent from this data that HDA is not a limiting reactant in the CI+RCOOH reaction, as HDA is not entirely consumed in mixtures where $X_{HDA} << 0.5$. Instead, a non-zero limiting value of HDA is found at high ozone exposures, once most of the Tri has been consumed and CIs are no longer being produced directly from ozonolysis. This indicates that the reaction between the CIs and HDA (R2, Scheme 1B) must be slow enough to allow the other sinks for the CI (R3-R6) to compete. Since the range of relevant reactions of the CI is sufficiently constrained in this system, it is possible to quantify this competition in terms of the rate constants governing each pathway, as described below.

4. Discussion

4.1. Analytical Kinetic Model

An analytical kinetic model for the decay of HDA can be used to quantify the competitive CI reaction pathways in this system. The rate law for [HDA] is,

$$\frac{d[\mathrm{HDA}]}{dt} = -k_{\mathrm{AAHP}}[\mathrm{HDA}][\mathrm{CI}] \quad (1)$$

where k_{AAHP} is the bimolecular rate constant for the CI + HDA reactions that forms AAHP products. The corresponding rate law that describes the time dependence of [CI] is,

$$\frac{d[\mathrm{CI}]}{dt} = k_{\mathrm{O3}}[\mathrm{Tri}][\mathrm{O_3}] - [\mathrm{CI}](k_{\mathrm{iso}} + k_{\mathrm{VHP}} + k_{\mathrm{H2O}}[\mathrm{H_2O}] + k_{\mathrm{AAHP}}[\mathrm{HDA}]) \quad (2)$$

where k_{O3} is the bimolecular rate constant for alkene ozonolysis assuming that POZ decomposition is not rate-limiting (R1, Scheme 1A). k_{iso} and k_{VHP} (R3–R4, Scheme 1B) are the unimolecular rate constants for isomerization to the carboxylic acid and the VHP intermediate, respectively, and k_{H2O} is the bimolecular rate constant for reaction with water to form HHPs (R5). As mentioned in the previous section, some potential sinks for HDA and CI, as well as the effects of volatile product evaporation, are assumed here to be negligible for the sake of simplicity. A

more complete mechanism, derived from Zeng's previous work,[12] is implemented in the stochastic kinetic simulations discussed in Section 4.3 and accounts for radical chain reactions and the evaporation of volatile products. The agreement between the stochastic kinetic simulations and the predictions of the model derived here is discussed in Section 4.4.

To find an expression for the [CI], a steady-state approximation is made (e.g., that [CI] will remain small and roughly constant for the duration of the reaction) which yields the following expression:

$$[\mathrm{CI}]_{\mathrm{ss}} = \frac{k_{\mathrm{O3}}[\mathrm{Tri}][\mathrm{O_3}]}{k_{\mathrm{uni}}+k_{\mathrm{H2O}}[\mathrm{H_2O}]+k_{\mathrm{AAHP}}[\mathrm{HDA}]} \quad (3)$$

where the two unimolecular rate constants are combined such that $k_{\mathrm{uni}} = k_{\mathrm{iso}} + k_{\mathrm{VHP}}$. Although the steady state assumption breaks down when there is a strong time-dependence to the intermediate concentration, the steady-state approach taken here can be justified by pseudo-first order rate analysis. For the case of neat Tri + O_3, the production rate governed by ozonolysis of the alkene (first term of Eq. 2) can be calculated via Eq. 5 below to be approximately 0.01 s^{-1}. As this is several orders of magnitude smaller than the combined CI loss rate (second term of Eq. 2), thought to be on the order of 10^2 s^{-1},[20] the CI are expected to reach their maximum concentration rapidly. Recent experimental evidence[28] has indicated that CI remain detectable for minutes after their formation in viscous secondary organic aerosol, longer than the 39 sec. flow tube residence time in this work, suggesting that the CI population may not deviate far from a steady state concentration over the duration of the measurements reported here. In addition, as discussed in Section 4.3, the results of this simple kinetic model agree with explicit kinetic simulations where no such steady-state assumptions are made.

The term describing the reaction with HDA in Eq. 3 can then be considered a perturbation to the equilibrium concentration of CI, and the system of equations can be solved self-consistently. Substitution of Eq. 3 into Eq. 1 yields,

$$\frac{d[\mathrm{HDA}]}{dt} = \frac{-k_{\mathrm{AAHP}}[\mathrm{HDA}]\cdot k_2[\mathrm{Tri}][\mathrm{O_3}]}{k_{\mathrm{uni}}+k_{\mathrm{H2O}}[\mathrm{H_2O}]+k_{\mathrm{AAHP}}[\mathrm{HDA}]} \tag{4}$$

For simplicity, the decay of Tri is approximated as an exponential function (i.e. $e^{-k_{rxn}\cdot t}$). Although the decay of Tri is generally non-exponential (see Fig. S7), an exponential approximation holds sufficiently well for small ozone exposures and is used to calculate uptake coefficients. Since the ozone concentration is constant during the reaction, the heterogeneous rate constant (k_{rxn}) can be expressed as,

$$k_{\mathrm{rxn}} = k_{O3}[\mathrm{O_3}] = \frac{6\cdot\gamma\cdot\bar{c}\cdot M}{4\cdot D_p\cdot\rho_0\cdot N_A}[\mathrm{O_3}] \tag{5}$$

where $\bar{c}$ is the mean speed of ozone, M is the molar mass of Tri (322 g/mol), D_p is the particle diameter, ρ_0 is the density of Tri (~1.5x10^{21} molec./cm^3), and N_A is Avogadro's number. Integrating Eq. 4 then yields the following expression for the time-dependence of HDA:

$$[\mathrm{HDA}](t) = \left(\frac{1}{k'}\right)\cdot W_0\left\{k'[\mathrm{HDA}]_0\cdot exp\left(k'\cdot\left([\mathrm{HDA}]_0 + [\mathrm{Tri}]_0(e^{-k_{\mathrm{rxn}}\cdot t}-1)\right)\right)\right\} \tag{6}$$

$$k' = \frac{k_{\mathrm{AAHP}}}{k_{\mathrm{uni}}+k_{\mathrm{H2O}}[H_2O]} \tag{7}$$

where $[\mathrm{HDA}]_0$ and $[\mathrm{Tri}]_0$ are the initial concentrations of HDA and Tri, respectively, and $W_0\{x\}$ is the principal branch of the Lambert W-function. The Lambert W-Function is a non-elementary function that has been used to provide analytical solutions to differential equations in chemical kinetics, notably in enzyme kinetics, and its implementations are readily available in Mathematica, Python, Matlab, and other platforms. Eq. 6 suggests that the relevant kinetic parameter controlling

the decay of HDA is *k'*, the ratio of the CI + RCOOH bimolecular rate constant to the sum of the first-order loss rates for the CI.

4.2. Fitting Analytical Model to HDA Decay

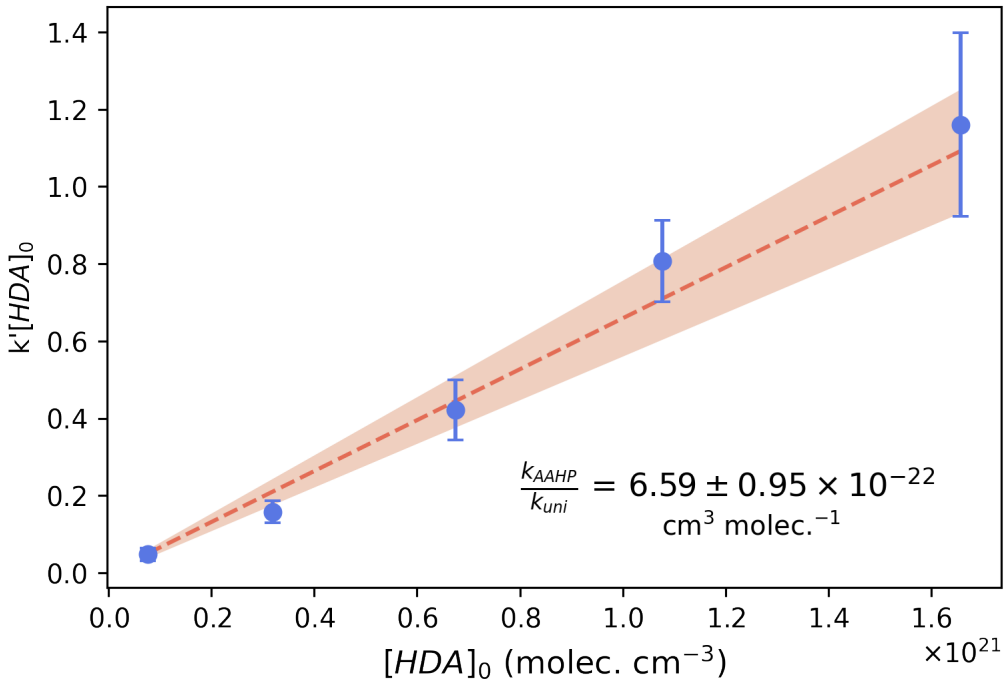

Figure 5: Pseudo-first order plot of fitted k'$[HDA]_0$ values (unitless) versus initial HDA concentration in each aerosol mixture. Points represent the mean value of k'$[HDA]_0$ obtained from fits to the experimental data in Fig. 4. Error bars represent ±1 standard deviation from the mean. The dashed line represents a linear fit to these points, with the slope of the line estimating the value of k' to be 6.59 ±

By normalizing the expression in Eq. 6 to $[HDA]_0$, the equation can be directly compared to the experimental data in Fig. 4. Of the four parameters in Eq. 6, $[Tri]_0$ and $[HDA]_0$ are related by the bulk densities and mole fractions of the organic mixture, and k_{rxn} is obtained from the observed decay of Tri, leaving *k'* as the sole adjustable parameter. The quantity $k'[HDA]_0$ is extracted from each experimental dataset in Fig. 4 through non-linear fitting, implemented in Python with the *scipy.optimize.curve_fit* function. The corresponding best fits to the aggregated experimental data are shown in Fig. 4 as dotted lines. The average values of $k'[HDA]_0$ retrieved from each fit are plotted in Fig. 5 as a function of $[HDA]_0$ and exhibit a linear relationship.

Analogous to a pseudo-first order method of determining a rate constant, the slope of the best fit line through the points in Fig. 5 is found yielding k' = 6.59 ± 0.95 x 10^{-22} cm^3 $molec.^{-1}$

Despite its rather simple assumptions, the analytical model provides an excellent fit to the experimental data. Although the value of k' fixes only a ratio of rate constants and not their absolute value, the k' derived from the fit in Fig. 5 may be combined with theoretical estimates of the unimolecular and CI-water rate constants to make a prediction about the magnitude of k_{AAHP}. The structure activity relationships (SAR) of Vereecken et al.[20] show that for primary ethyl or propyl CI in the *anti* conformation, the isomerization channel to produce acids (R4, Scheme 1B) has a rate constant of 74 s^{-1}, whereas for the *syn* conformation, the isomerization to the VHP intermediate (R3) has a rate constant of 205 s^{-1}. Since the experiments are conducted using dry gases without introducing water vapor, the loss of CI to water (R5) is assumed to be negligible. Zeng assumed a small but non-zero RH value (~3%) in dry experiments to account for the potential of ambient water in the flow system and, using the k_{H2O} calculated by Vereecken,[20] estimated the $k_{H2O}[H_2O]$ term to be roughly 2 s^{-1}.[12] Combining the first-order loss rates yields $k_{uni} + k_{H2O}[H_2O]$ as 281 s^{-1}, and multiplying this value by k' yields k_{AAHP} = 1.85 ± 0.27 x 10^{-19} cm^3 $molec.^{-1}$ sec^{-1}.

Compared to the gas phase, where k_{AAHP} has been measured to exceed 10^{-10} cm^3 $molec.^{-1}$ $sec.^{-1}$, the value of the rate constant derived here is quite small, but not without precedent. Interestingly, although they allow the value of k_{AAHP} to vary between datasets in their model of oleic acid ozonolysis, Gallimore and co-workers report a ratio k_{AAHP}/k_{uni} of 5x10^{-22} cm^3 $mol.^{-1}$ (0.3 M^{-1}), and fix k_{uni} at 500 s^{-1} based on empirical measurements, a factor of 2 greater than the k_{uni} determined here.[10] Using Gallimore's parameters, the resulting value of k_{AAHP} is 2.5x10^{-19} cm^3 $molec.^{-1}$ $sec.^{-1}$, in excellent agreement with the estimate provided above. In Berkemeier *et al.*, although a specific value of k_{AAHP} was not reported, k_{AAHP} was allowed to vary between 10^{-18}–

10^{-12} cm^3 $molec.^{-1}$ $sec.^{-1}$, the lower bound lying just above the empirical estimate derived from Fig. 5.[11]

4.3. Stochastic Kinetic Simulations

To test the assumptions made in the derivation of Eq. (6) we use a stochastic kinetic simulation using the explicit mechanism developed by Zeng.[12] This mechanism includes ·OH production during multiphase ozonolysis, which is neglected in the derivation of Eq. 6. The production of ·OH and other radicals were identified as significant reactive sink for Tri during multiphase ozonolysis. As shown by Zeng, the ·OH radical produced by the decomposition of the CI can add to a C=C bond to form a β-hydroxy RO_2 radical.[18] As first reported by Beauchamp and coworkers,[29] this β-hydroxy RO_2 radical can, in turn, reform CIs, via a mechanism that is currently unclear.[30] While the empirical decay rate of Tri employed in this model should partially account for additional Tri consumption by ·OH radicals, Eq. 6 does not account for the production of CI via the β-RO_2 pathway. Additionally, other potentially important reactive sinks for CI, such as its direct reaction with ozone are also not included in the derivation of Eq. 6. (These reactions are not shown in Scheme 1 but are detailed in Table S2 in the Supporting Information.) To evaluate the reasonableness of the model derived in Section 4.1 and the corresponding estimate of k_{AAHP}, explicit stochastic simulations of the system are run in Kinetiscope,[31] an open-source software package that implements a kinetic Monte Carlo algorithm for a user-defined reaction mechanism. Multiple previous studies have used models built in Kinetiscope to accurately describe heterogeneous chemistry in aerosols, including Tri ozonolysis in the presence of a CI scavenger.[12,32,33]

The previously-developed simulation framework has been adapted to the current reaction and the full mechanism is described Table S2 (Supplementary Information). In particular, the

isomerization of CI to form acids (R4) is included, to explain the product acids observed in Fig. 2. The reaction between HDA and the ·OH radicals produced from CI decomposition makes a small contribution to the decay kinetics of HDA, and so is also included. Following Zeng's previous studies of Tri ozonolysis,[12,18] the formation of secondary ozonide (SOZ) products (Scheme 1B, R6) is not included as they were not observed under multiple ionization methods. Although equilibrium partitioning calculations[13] predict that some tetradecanal may remain in the particle available for reaction, model sensitivity tests including this pathway are out of agreement with experimental results, as detailed in Fig. S5 of the Supporting Information. Finally, the evaporation of nonanal (R14) is allowed in the simulation to account for the slight change in particle diameter observed over the course of the reaction. As discussed by Müller et al. in the context of oleic acid ozonolysis,[34] reaction time and oxidant exposure may not be equivalent measures of reaction progress in experiments involving high oxidant concentrations, owing to the evaporation of volatile products. Since the experimental kinetic data presented here is measured in terms of oxidant exposure and involves high (ppm) oxidant concentrations, the inclusion of evaporation steps in the stochastic model is important for validating the value of k_{AAHP} derived from experiment. A comparison of the simulated and observed particle diameter for neat Tri aerosol and for each of the binary mixtures in this study is shown in Fig. S6, and the agreement between stochastic model predictions and other experimental observations is discussed below.

The value of k_{AAHP} is treated as the sole adjustable parameter in the model, allowing for direct evaluation of the reasonableness of the rate constant derived from Eq. 6. Shown in Fig. 3 are two modeling scenarios using two different values for k_{AAHP}. In Scenario A, the value of k_{AAHP} is chosen to be 2.2×10^{-19} cm^3 $molec.^{-1}$ $sec.^{-1}$, which lies just beyond one standard deviation from the mean of the empirical estimate given in the previous section. This value was chosen to produce

the best qualitative agreement with the data in Fig. 4. The uptake coefficients predicted under Scenario A are represented by the vertices of the solid line in Fig. 3. Scenario A closely reproduces both the observed uptake coefficients and the decay kinetics of Tri (Fig. S7).

By contrast, k_{AAHP} is fixed at $1x10^{-13}$ cm^3 $molec.^{-1}$ $sec.^{-1}$ in Scenario B, to represent the CI+RCOOH reaction occurring at a rate near the diffusion limit. Uptake coefficients corresponding to this scenario are represented by the dashed line in Fig. 3, which deviates sharply from the experimental results at low HDA fractions and flattens once X_{HDA} exceeds 50%. Fig. S8 shows the Tri decay kinetics corresponding to these predictions, which exhibit a linear initial consumption rate of Tri, followed by sharp transition to a region of non-linear decay. The simulated decay of HDA in Fig. S9 explains these unphysical predictions: when X_{HDA} is below 50%, a CI + RCOOH reaction occurring at the diffusion limit far outcompetes all other CI sinks, resulting in a zero-order (linear) decay of HDA until it is consumed. Once X_{HDA} exceeds 50%, the uptake is limited primarily by the amount of Tri available, and further increases in HDA have minimal impact on the uptake coefficient. As scenario B clearly does not describe the observed trend in γ_{eff} or in the decay of HDA, a rate constant near the diffusion limit can be ruled out. Additionally, to ensure that the simulation results were sufficiently sensitive to allow specification of k_{AAHP}, simulations were run with values of k_{AAHP} both an order of magnitude greater and an order of magnitude smaller than the value specified in Scenario A. The resulting values of γ_{eff} and simulated decay traces for X_{HDA} = 20%can be seen in Fig. S10.

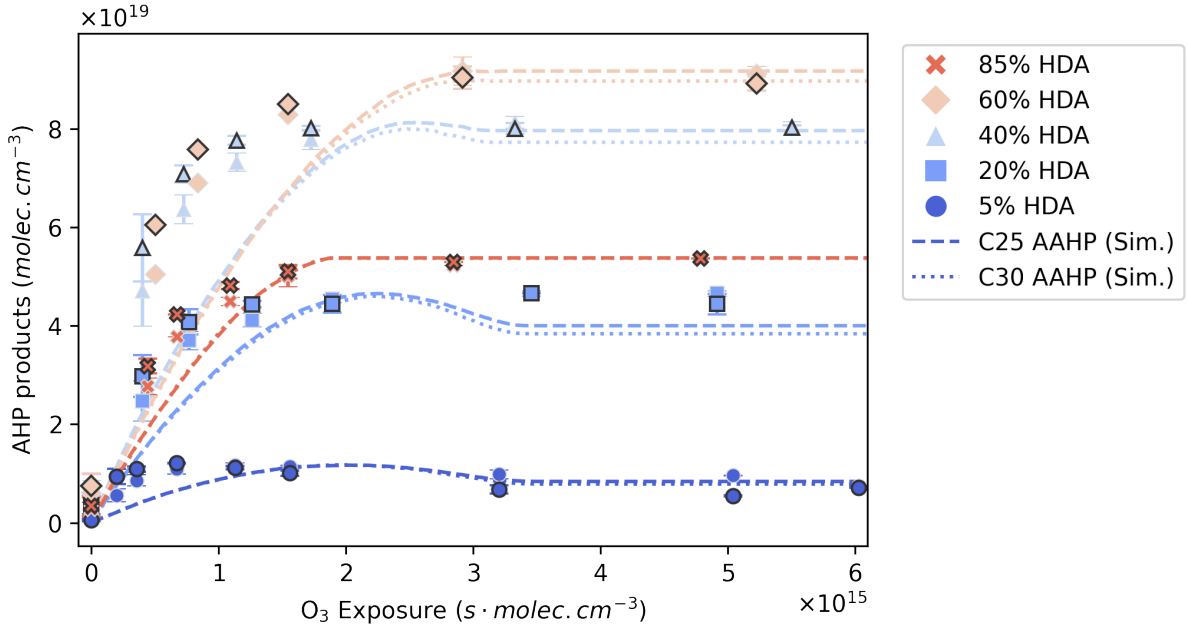

Figure 6: The kinetic evolution of AAHP reaction products at each HDA mole fraction, comparing experimental observations (points) to the results of explicit kinetic simulations under Scenario A (solid lines). Observations correspond to integrated intensities of mass spectral peaks corresponding to AAHP products. Light-outlined points correspond to C25 AAHPs (m/z = 397 in positive ion mode and m/z = 669 in negative ion mode), and dark-outlined points correspond to C30 AAHPs (m/z = 467 in positive ion mode and m/z = 739 in negative ion mode); see Section 3.1. Experimental data is scaled to match the maximum product concentration of each simulation result.

Further supporting the choice of rate constant in Scenario A, Fig. 6 shows the observed kinetics of the AAHP products overlaid with the kinetics predicted by Scenario A. At the lowest HDA mole fraction (5%), the experimental observation shows the AAHP products reach a peak concentration before then decaying gradually. This behavior is captured in the corresponding simulation results, where once the AAHP products form they are consumed by radicals. Agreement between this simulation and experimental results is acceptable for the scenarios where X_{HDA} is less than 50%, and is generally better than the corresponding prediction by Scenario B (Fig. S11). When X_{HDA} is greater than 50%, a larger discrepancy between the experimental data and the model prediction arises and is evident for the 85% X_{HDA} case. This discrepancy seems to arise from the

description of Tri decay kinetics (Fig. S7). One potential explanation for this discrepancy is the implicit assumptions governing ozone adsorption in the model. The current framework assumes that the number of adsorption sites on the surface of the particle is proportional solely to the mole fraction of Tri in the mixture. As more HDA is incorporated in an aerosol particle, fewer and fewer ozone adsorption sites are allowed, up to the limit that no adsorption sites are allowed for a pure HDA particle. The agreement between simulation and experiment at high X_{HDA} could be improved by allowing HDA to contribute adsorption sites, consistent with studies that suggest significant amounts of ozone adsorb to nonreactive fatty acid aerosols.[35,36] However, this modification has not been implemented in the present study to allow for ease of comparison with previously published modeling results.[12]

4.4. Comparison of Analytical & Stochastic Models

Both the explicit simulations and the analytical model indicate that the CI + RCOOH rate constant is on the order of 10^{-19} cm^3 $molec.^{-1}$ $sec.^{-1}$, 9 orders of magnitude smaller than the gas phase rate constant. Assuming that the rate were limited only by reactant diffusion in the condensed phase, the expected rate constant would be 3.6×10^{-13} cm^3 $molec.^{-1}$ $sec.^{-1}$, given an organic liquid with viscosity of 15 mPa·s and reactant collisional radii of 2 nm. This diffusion-controlled rate coefficient is still significantly faster than the rate estimated by the kinetic analysis in this study. Several theoretical studies of this reaction in the gas phase concur that the prevailing entrance channel for the two reactants is barrierless, and leads to direct formation of the AAHP product via 1,4 addition, with formation of a pre-reactive complex not significantly contributing to the overall kinetics of the reaction.[19,37] Thus, it seems likely that entropic effects are significant in limiting this reaction in the condensed-phase. In particular, Vereecken reported that the approach geometry

is a significant factor in determining reaction favorability, with preferred geometries having both molecules coplanar.[19]

This apparent deceleration of a rapid gas phase bimolecular CI reaction when conducted in an aerosol is not without precedent. Heine and co-workers discussed a similar discrepancy between observations and gas-phase estimates for CI cycloaddition to carbonyl (C=O) functionalities to form secondary ozonides during a modeling study of squalene ozonolysis.[32] There, CI + C=O reaction rates were optimized to reproduce the observed SOZ formation kinetics, converging on two values for the rate constant: 6.7×10^{-19} cm^3 $molec.^{-1}$ $sec.^{-1}$ in cases where the CI and C=O reactants are formed from different POZs, and a rate two times faster when the reactants are formed from decomposition of the same POZ. This effect is analogous to that observed for peroxy radical recombination rates,[38] where the organic matrix forms a "solvent cage" that increases the interaction time of reactants formed in proximity to one another, while reactants formed in separate cages must overcome a barrier before encountering another reactant by diffusion. The lipidic chains of Tri and HDA likely provide a similar solvation environment in the present system, forming an aliphatic shell that nascent CIs must disrupt before encountering and reacting with a nearby HDA molecule.

5. Conclusion

The experimental data and modeling results presented here suggest that a reasonable rate constant for the CI + RCOOH reaction in the condensed phase of an organic aerosol should be much slower than the diffusion limit in the condensed phase. The monotonic decrease in the reactive uptake coefficient of O_3 by Tri as more HDA is incorporated into the aerosol indicates that the CI + RCOOH reaction behaves as a CI scavenger, outcompeting the unimolecular decay process by which CIs produce ·OH radicals and initiate radical chain chemistry. Direct

observations of the decay of HDA in the presence of Tri and O_3 confirm this hypothesis and show that HDA is not a limiting reactant over the range of mole fractions studied here. The decay kinetics of HDA are governed by the production and multifaceted consumption of CI from ozonolysis, which lends itself to a simple kinetic model from which the ratio k_{AAHP}/k_{uni} can be extracted. Multiplying by a theoretical estimate of the unimolecular decay rate of CI, the CI + RCOOH rate constant is found to be $1.85 \pm 0.27 \times 10^{-19}$ cm^3 $molec.^{-1}$ $sec.^{-1}$. Explicit kinetic simulations using a value in this range agree well with experimental data.

Given the large difference between this rate coefficient and gas-phase measurements, further condensed-phase kinetic studies, such as in aqueous environments, may be valuable in understanding how this rate depends upon the solvation environment and the ultimate relevance of this reaction to the processing of atmospheric aerosol. In contrast to the gas phase, where the CI + RCOOH reaction is expected to be a major reactive sink of CI, acids may not outcompete other CI reaction partners in more viscous condensed phases. As a result, careful measurements of other slow bimolecular reactions of CI in non-aqueous condensed phases may be of value. The similarity of the rate constant estimated here for the CI + RCOOH reactions to the rate constants adopted for CI + alcohols and CI + carbonyls in previous organic systems suggests that the composition of the condensed phase could be the most important factor in determining the rates of bimolecular reactions of CI in organic aerosol. Finally, the formation of oligomeric AAHP species as a mechanism for particle growth should be analyzed more carefully, as heterogeneous reactions between CI and acids may kinetically outcompete the corresponding homogeneous process.

Supporting Information: Figures S1-S11: Experimental set-up and diagram of modified APCI source, CID mass spectra of negative ion clusters, particle diameter changes and decay kinetics of Tri, simulation results from Scenario B, and sensitivity tests of model parameters. Table S1: Summary of experimental conditions and kinetic observations (particle diameters, uptake coefficients). Table S2: Mechanism of Tri ozonolysis and secondary chemistry, including kinetic parameters used in explicit simulations.

Acknowledgements: We thank Meirong Zeng for helpful discussions. This work was supported by the Gas Phase Chemical Physics Program (GPCP), in the Chemical Sciences Geosciences and Biosciences Division of the Office of Basic Energy Sciences of the U.S. Department of Energy under Contract No. DE-AC02-05CH11231.

References

(1) Taatjes, C. A. Criegee Intermediates: What Direct Production and Detection Can Teach Us About Reactions of Carbonyl Oxides. *Annu. Rev. Phys. Chem.* **2017**, *68* (1), 183–207. https://doi.org/10.1146/annurev-physchem-052516-050739.

(2) Taatjes, C. A.; Welz, O.; Eskola, A. J.; Savee, J. D.; Scheer, A. M.; Shallcross, D. E.; Rotavera, B.; Lee, E. P. F.; Dyke, J. M.; Mok, D. K. W.; Osborn, D. L.; Percival, C. J. Direct Measurements of Conformer-Dependent Reactivity of the Criegee Intermediate CH3CHOO. *Science* **2013**, *340* (6129), 177–180. https://doi.org/10.1126/science.1234689.

(3) A. Taatjes, C.; Welz, O.; J. Eskola, A.; D. Savee, J.; L. Osborn, D.; F. Lee, E. P.; M. Dyke, J.; K. Mok, D. W.; E. Shallcross, D.; J. Percival, C. Direct Measurement of Criegee Intermediate (CH 2 OO) Reactions with Acetone , Acetaldehyde , and Hexafluoroacetone. *Physical Chemistry Chemical Physics* **2012**, *14* (30), 10391–10400. https://doi.org/10.1039/C2CP40294G.

(4) Welz, O.; Eskola, A. J.; Sheps, L.; Rotavera, B.; Savee, J. D.; Scheer, A. M.; Osborn, D. L.; Lowe, D.; Murray Booth, A.; Xiao, P.; Anwar H. Khan, M.; Percival, C. J.; Shallcross, D. E.; Taatjes, C. A. Rate Coefficients of C1 and C2 Criegee Intermediate Reactions with Formic and Acetic Acid Near the Collision Limit: Direct Kinetics Measurements and Atmospheric Implications. *Angewandte Chemie* **2014**, *126* (18), 4635–4638. https://doi.org/10.1002/ange.201400964.

(5) Chhantyal-Pun, R.; Welz, O.; Savee, J. D.; Eskola, A. J.; Lee, E. P. F.; Blacker, L.; Hill, H. R.; Ashcroft, M.; Khan, M. A. H.; Lloyd-Jones, G. C.; Evans, L.; Rotavera, B.; Huang, H.; Osborn, D. L.; Mok, D. K. W.; Dyke, J. M.; Shallcross, D. E.; Percival, C. J.; Orr-Ewing, A. J.; Taatjes, C. A. Direct Measurements of Unimolecular and Bimolecular Reaction Kinetics of the Criegee Intermediate $(CH_3)_2COO$. *J. Phys. Chem. A* **2017**, *121* (1), 4–15. https://doi.org/10.1021/acs.jpca.6b07810.

(6) Katrib, Y.; Biskos, G.; Buseck, P. R.; Davidovits, P.; Jayne, J. T.; Mochida, M.; Wise, M. E.; Worsnop, D. R.; Martin, S. T. Ozonolysis of Mixed Oleic-Acid/Stearic-Acid Particles: Reaction Kinetics and Chemical Morphology. *J. Phys. Chem. A* **2005**, *109* (48), 10910–10919. https://doi.org/10.1021/jp054714d.

(7) Zhou, S.; Joudan, S.; Forbes, M. W.; Zhou, Z.; Abbatt, J. P. D. Reaction of Condensed-Phase Criegee Intermediates with Carboxylic Acids and Perfluoroalkyl Carboxylic Acids. *Environ. Sci. Technol. Lett.* **2019**, *6* (4), 243–250. https://doi.org/10.1021/acs.estlett.9b00165.

(8) Katrib, Y.; Martin, S. T.; Hung, H.-M.; Rudich, Y.; Zhang, H.; Slowik, J. G.; Davidovits, P.; Jayne, J. T.; Worsnop, D. R. Products and Mechanisms of Ozone Reactions with Oleic Acid for Aerosol Particles Having Core−Shell Morphologies. *J. Phys. Chem. A* **2004**, *108* (32), 6686–6695. https://doi.org/10.1021/jp049759d.

(9) Ziemann, P. J. Aerosol Products, Mechanisms, and Kinetics of Heterogeneous Reactions of Ozone with Oleic Acid in Pure and Mixed Particles. *Faraday Discuss.* **2005**, *130* (0), 469–490. https://doi.org/10.1039/B417502F.

(10) Gallimore, P. J.; Griffiths, P. T.; Pope, F. D.; Reid, J. P.; Kalberer, M. Comprehensive Modeling Study of Ozonolysis of Oleic Acid Aerosol Based on Real-Time, Online Measurements of Aerosol Composition. *Journal of Geophysical Research: Atmospheres* **2017**, *122* (8), 4364–4377. https://doi.org/10.1002/2016JD026221.

(11) Berkemeier, T.; Mishra, A.; Mattei, C.; Huisman, A. J.; Krieger, U. K.; Pöschl, U. Ozonolysis of Oleic Acid Aerosol Revisited: Multiphase Chemical Kinetics and Reaction Mechanisms. *ACS Earth Space Chem.* **2021**, *5* (12), 3313–3323. https://doi.org/10.1021/acsearthspacechem.1c00232.
(12) Zeng, M.; Wilson, K. R. Efficient Coupling of Reaction Pathways of Criegee Intermediates and Free Radicals in the Heterogeneous Ozonolysis of Alkenes. *J. Phys. Chem. Lett.* **2020**, *11* (16), 6580–6585. https://doi.org/10.1021/acs.jpclett.0c01823.
(13) Pankow, J. F. An Absorption Model of Gas/Particle Partitioning of Organic Compounds in the Atmosphere. *Atmospheric Environment* **1994**, *28* (2), 185–188. https://doi.org/10.1016/1352-2310(94)90093-0.
(14) Roveretto, M.; Li, M.; Hayeck, N.; Brüggemann, M.; Emmelin, C.; Perrier, S.; George, C. Real-Time Detection of Gas-Phase Organohalogens from Aqueous Photochemistry Using Orbitrap Mass Spectrometry. *ACS Earth Space Chem.* **2019**, *3* (3), 329–334. https://doi.org/10.1021/acsearthspacechem.8b00209.
(15) Adas, F.; Picart, D.; Berthou, F.; Simon, B.; Amet, Y. Liquid Chromatography–Mass Spectrometry and Gas Chromatography–Mass Spectrometry of v- and (v-1)-Hydroxylated Metabolites of Elaidic and Oleic Acids in Human and Rat Liver Microsomes. *J. Chromatogr. B* **1998**, 12.
(16) Byrdwell, W. C. Atmospheric Pressure Chemical Ionization Mass Spectrometry for Analysis of Lipids. *Lipids* **2001**, *36* (4), 327–346. https://doi.org/10.1007/s11745-001-0725-5.
(17) Bell, S. E.; Ewing, R. G.; Eiceman, G. A.; Karpas, Z. Atmospheric Pressure Chemical Ionization of Alkanes, Alkenes, and Cycloalkanes. *J. Am. Soc. Mass Spectrom.* **1994**, *5* (3), 177–185. https://doi.org/10.1016/1044-0305(94)85031-3.
(18) Zeng, M.; Heine, N.; Wilson, K. R. Evidence That Criegee Intermediates Drive Autoxidation in Unsaturated Lipids. *PNAS* **2020**. https://doi.org/10.1073/pnas.1920765117.
(19) Vereecken, L. The Reaction of Criegee Intermediates with Acids and Enols. *Phys. Chem. Chem. Phys.* **2017**, *19* (42), 28630–28640. https://doi.org/10.1039/C7CP05132H.
(20) Vereecken, L.; Novelli, A.; Taraborrelli, D. Unimolecular Decay Strongly Limits the Atmospheric Impact of Criegee Intermediates. *Phys. Chem. Chem. Phys.* **2017**, *19* (47), 31599–31612. https://doi.org/10.1039/C7CP05541B.
(21) Enami, S. Fates of Organic Hydroperoxides in Atmospheric Condensed Phases. *J. Phys. Chem. A* **2021**. https://doi.org/10.1021/acs.jpca.1c01513.
(22) Zeng, M.; Wilson, K. R. Experimental Evidence That Halogen Bonding Catalyzes the Heterogeneous Chlorination of Alkenes in Submicron Liquid Droplets. *Chem. Sci.* **2021**, *12* (31), 10455–10466. https://doi.org/10.1039/D1SC02662C.
(23) Wilson, K. R.; Smith, J. D.; Kessler, S. H.; Kroll, J. H. The Statistical Evolution of Multiple Generations of Oxidation Products in the Photochemical Aging of Chemically Reduced Organic Aerosol. *Phys. Chem. Chem. Phys.* **2012**, *14* (4), 1468–1479. https://doi.org/10.1039/C1CP22716E.
(24) Smith, J. D.; Kroll, J. H.; Cappa, C. D.; Che, D. L.; Liu, C. L.; Ahmed, M.; Leone, S. R.; Worsnop, D. R.; Wilson, K. R. The Heterogeneous Reaction of Hydroxyl Radicals with Sub-Micron Squalane Particles: A Model System for Understanding the Oxidative Aging of Ambient Aerosols. *Atmos. Chem. Phys.* **2009**, 14.
(25) Liu, C.-L.; Smith, J. D.; Che, D. L.; Ahmed, M.; Leone, S. R.; Wilson, K. R. The Direct Observation of Secondary Radical Chain Chemistry in the Heterogeneous Reaction of

Chlorine Atoms with Submicron Squalane Droplets. *Phys. Chem. Chem. Phys.* **2011**, *13* (19), 8993. https://doi.org/10.1039/c1cp20236g.
(26) Wells, J. R.; Morrison, G. C.; Coleman, B. K.; Spicer, C.; Dean, S. W. Kinetics and Reaction Products of Ozone and Surface-Bound Squalene. *J. ASTM Int.* **2008**, *5* (7), 101629. https://doi.org/10.1520/JAI101629.
(27) Atkinson, R. Estimations of OH Radical Rate Constants from H-Atom Abstraction from C□H and O□H Bonds over the Temperature Range 250-1000 K. *International Journal of Chemical Kinetics* **1986**, *18* (5), 555–568. https://doi.org/10.1002/kin.550180506.
(28) Campbell, S. J.; Wolfer, K.; Gallimore, P. J.; Giorio, C.; Häussinger, D.; Boillat, M.-A.; Kalberer, M. Characterization and Quantification of Particle-Bound Criegee Intermediates in Secondary Organic Aerosol. *Environ. Sci. Technol.* **2022**, *56* (18), 12945–12954. https://doi.org/10.1021/acs.est.2c04101.
(29) Zhang, X.; Barraza, K. M.; Beauchamp, J. L. Cholesterol Provides Nonsacrificial Protection of Membrane Lipids from Chemical Damage at Air–Water Interface. *PNAS* **2018**, *115* (13), 3255–3260. https://doi.org/10.1073/pnas.1722323115.
(30) Wagner, J. P. Criegee Intermediates in Autoxidation Reactions: Mechanistic Considerations. *J. Phys. Chem. A* **2021**, *125* (1), 406–410. https://doi.org/10.1021/acs.jpca.0c09971.
(31) Hinsberg, W. D.; Houle, F. A. Kinetiscope – A Stochastic Kinetics Simulator, 2019. http://hinsberg.net/kinetiscope.
(32) Heine, N.; Houle, F. A.; Wilson, K. R. Connecting the Elementary Reaction Pathways of Criegee Intermediates to the Chemical Erosion of Squalene Interfaces during Ozonolysis. *Environ. Sci. Technol.* **2017**, *51* (23), 13740–13748. https://doi.org/10.1021/acs.est.7b04197.
(33) A. Wiegel, A.; R. Wilson, K.; D. Hinsberg, W.; A. Houle, F. Stochastic Methods for Aerosol Chemistry: A Compact Molecular Description of Functionalization and Fragmentation in the Heterogeneous Oxidation of Squalane Aerosol by OH Radicals. *Physical Chemistry Chemical Physics* **2015**, *17* (6), 4398–4411. https://doi.org/10.1039/C4CP04927F.
(34) Müller, M.; Mishra, A.; Berkemeier, T.; Hausammann, E.; Peter, T.; Krieger, U. K. Electrodynamic Balance–Mass Spectrometry Reveals Impact of Oxidant Concentration on Product Composition in the Ozonolysis of Oleic Acid. *Phys. Chem. Chem. Phys.* **2022**, *24* (44), 27086–27104. https://doi.org/10.1039/D2CP03289A.
(35) Kwamena, N.-O. A.; Staikova, M. G.; Donaldson, D. J.; George, I. J.; Abbatt, J. P. D. Role of the Aerosol Substrate in the Heterogeneous Ozonation Reactions of Surface-Bound PAHs. *J. Phys. Chem. A* **2007**, *111* (43), 11050–11058. https://doi.org/10.1021/jp075300i.
(36) Renbaum, L. H.; Smith, G. D. Artifacts in Measuring Aerosol Uptake Kinetics: The Roles of Time, Concentration and Adsorption. *Atmospheric Chemistry and Physics* **2011**, *11* (14), 6881–6893. https://doi.org/10.5194/acp-11-6881-2011.
(37) Long, B.; Cheng, J.-R.; Tan, X.; Zhang, W. Theoretical Study on the Detailed Reaction Mechanisms of Carbonyl Oxide with Formic Acid. *Journal of Molecular Structure: THEOCHEM* **2009**, *916* (1–3), 159–167. https://doi.org/10.1016/j.theochem.2009.09.028.
(38) Pryor, W. A.; Smith, K. Viscosity Dependence of Bond Homolysis. Qualitative and Semiquantitative Test for Cage Return. *J. Am. Chem. Soc.* **1970**, *92* (18), 5403–5412. https://doi.org/10.1021/ja00721a019.

Table of Contents (TOC) Graphic:

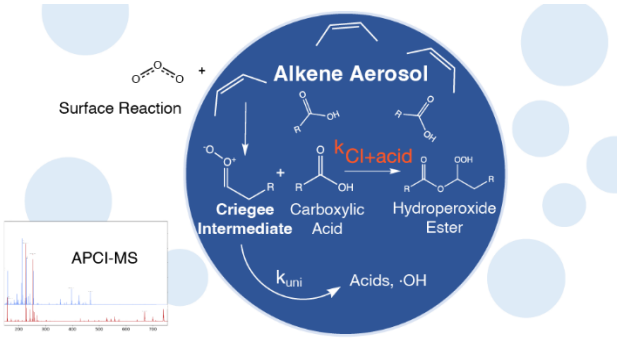

Supplementary Information for

Constraining the Reaction Rate of Criegee Intermediates with Carboxylic Acids during the Multiphase Ozonolysis of Aerosolized Alkenes

Ryan Reynolds,[1,2] Musahid Ahmed[1] and Kevin R. Wilson[1*]

[1]*Chemical Sciences Division, Lawrence Berkeley National Laboratory, Berkeley, CA, 94720, USA*

[2]*Department of Chemistry, University of California, Berkeley, CA 94720, USA*

Table S1. Experimental conditions and observations. D_p is average diameter and σ_g is the geometric standard deviation of the particle size distribution.

X_{Tri}	X_{HDA}	HDA:Tri	D_p (nm)	σ_g	k_{rxn} (cm^{-3} $molec.^{-1}$ $sec.^{-1}$)
100%	0	0	480, 434	1.29, 1.29	$6.74x10^{-4}$, $5.20x10^{-4}$
95%	5%	0.052	382, 309, 369, 268, 256	1.33, 1.37, 1.35, 1.38, 1.37	$6.43x10^{-4}$, $5.29x10^{-4}$, $6.21x10^{-4}$, $4.87x10^{-4}$, $3.92x10^{-4}$
80%	20%	0.25	279, 269, 255	1.39, 1.39, 1.38	$4.12x10^{-4}$, $5.33x10^{-4}$, $4.15x10^{-4}$
60%	40%	0.67	268, 253, 282, 247	1.53, 1.68, 1.67, 1.39	$3.16x10^{-4}$, $4.19x10^{-4}$, $3.73x10^{-4}$, $3.13x10^{-4}$
40%	60%	1.50	293, 271, 315	1.58, 1.56, 1.44	$2.47x10^{-4}$, $2.10x10^{-4}$, $2.15x10^{-4}$
15%	85%	5.67	266, 267, 265, 263	1.39, 1.42, 1.47, 1.39	$6.56x10^{-5}$, $6.79x10^{-5}$, $9.72x10^{-5}$, $6.26x10^{-5}$

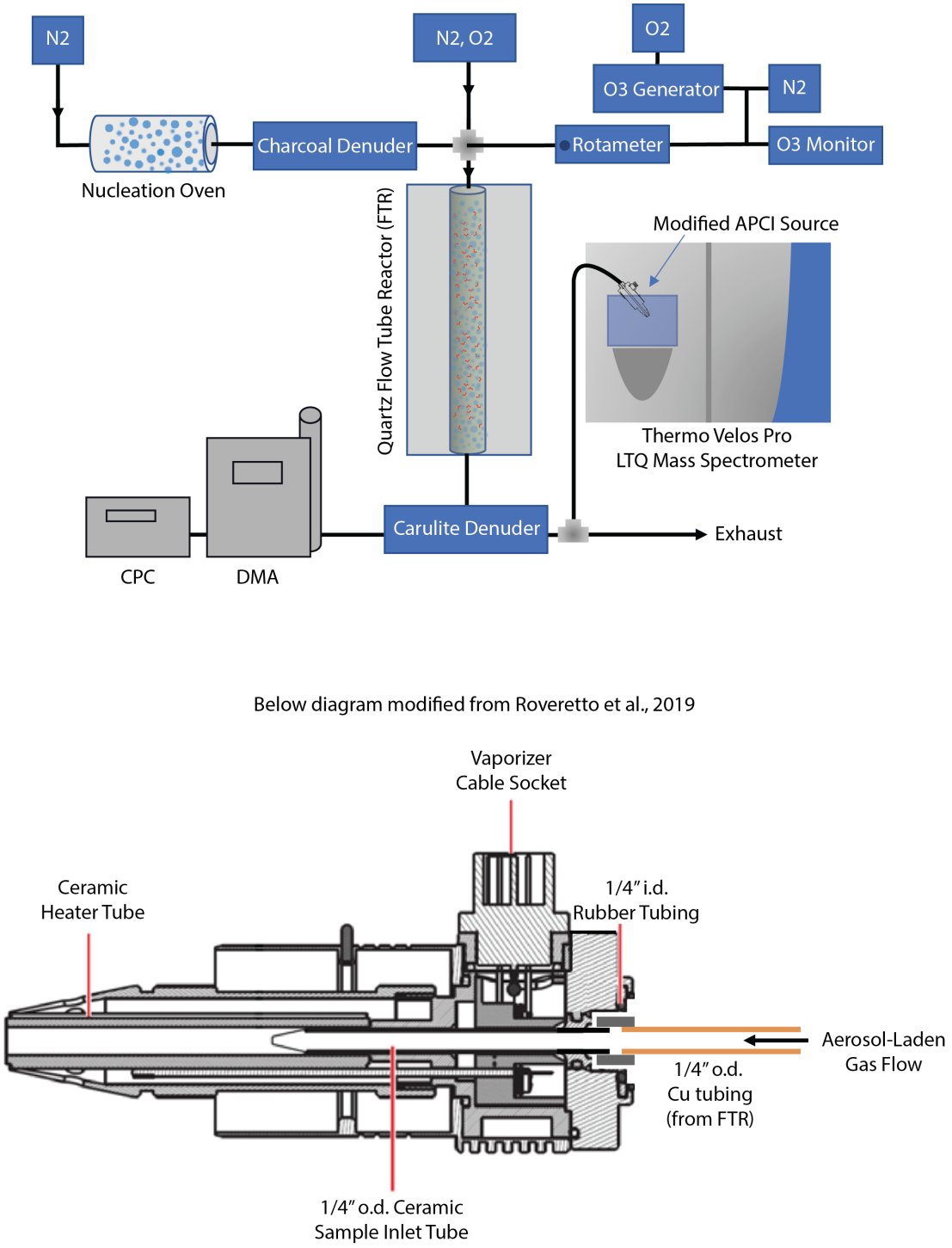

Figure S1: (*Above*) Diagram of experimental setup for all flow tube studies reported in Table S1 and the main text. (*Below*) Diagram of modified APCI source. Figure adapted from ThermoFisher LTQ Manual and the Supplementary Information of Roveretto et al., 2019.[1]

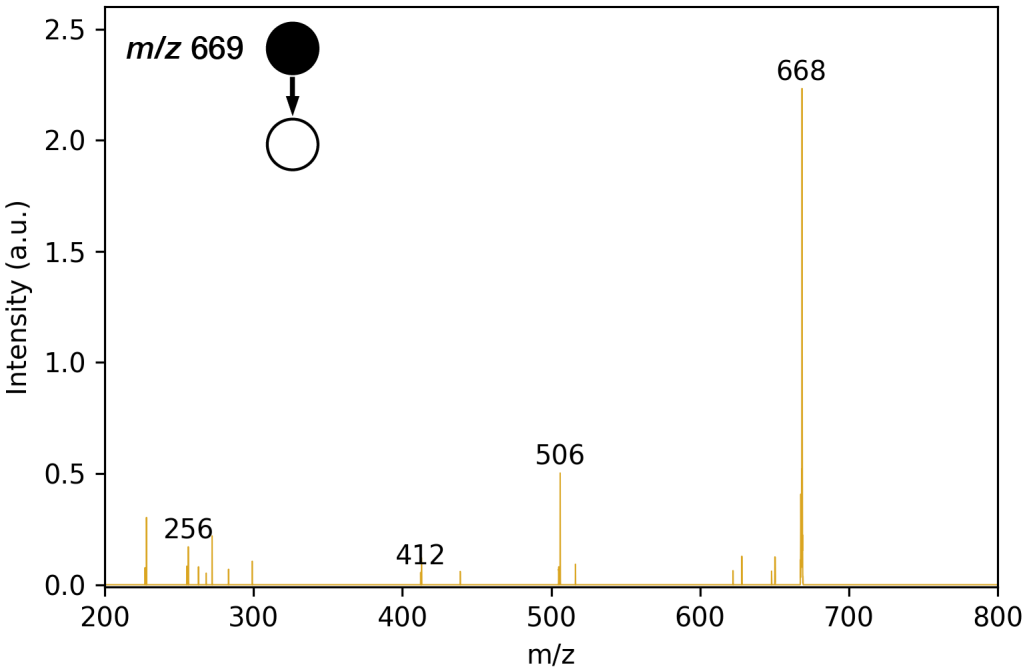

Figure S2: Collision-induced Dissociation (CID) of m/z 669 cluster peak in negative ion mode, showing evolution of an HDA molecule (m/z 256) and a reduced fragment corresponding to the AAHP (m/z 412, MW 414).

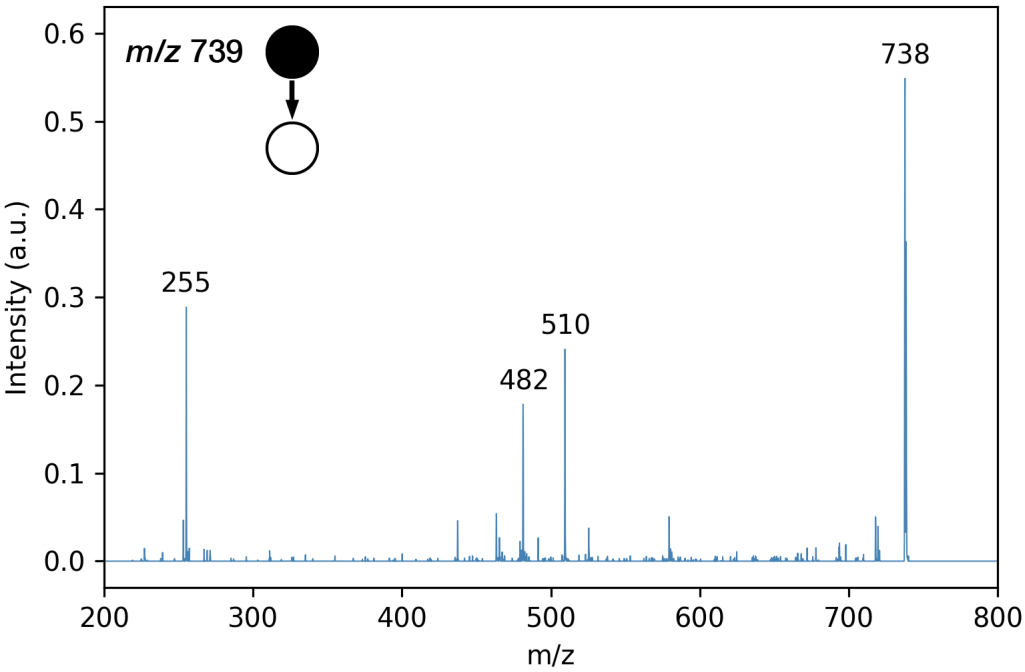

Figure S3: Collision-induced Dissociation (CID) of m/z 739 cluster peak in negative ion mode, showing evolution of an HDA molecule (m/z 255) and a reduced fragment corresponding to the AAHP (m/z = 482, MW 484).

Table S2. Reaction Mechanism.

Step No.	Reaction Step	Label (Analytical Model)	Value	Units	Reference (Notes)
	O_3 (g) -> O_3 (ads)		0.37	sec.$^{-1}$ (pseudo-first order, $[O_3]_g$=1ppm)	Calculated, see Ref.[2]
R1	O_3 (ads) + Tri -> CI + C=O		2x10^{-16}	cm^3 molec.$^{-1}$ sec.$^{-1}$	[2]
R3	CI -> RO· + ·OH	k_{VHP}	205	sec.$^{-1}$	[3]
R4	CI -> RCOOH	k_{iso}	74	sec.$^{-1}$	[3]
R2	CI + HDA -> AAHP	k_{AAHP}	2.1x10^{-19} *or* 1.0x10^{-13} (see text)	cm^3 molec.$^{-1}$ sec.$^{-1}$	This work
R5	CI + H2O -> HHP	$k_{\mathrm{H2O}}[\mathrm{H_2O}]$	2.17	sec.$^{-1}$ (pseudo-first order, RH = 3%)	[3]
(R6)	CI + RC=O -> SOZ	k_{SOZ}	n/a	n/a	[2] *(Not observed in this study)*
**	CI + O_3 (ads) -> C=O		1.0x10^{-13}	cm^3 molec.$^{-1}$ sec.$^{-1}$	[2] *(Only in explicit simulations)*
R7	·OH + Tri -> Tri-R· + H_2O		2.0x10^{-11}	cm^3 molec.$^{-1}$ sec.$^{-1}$	[4,5]
R8a	Tri-R· + O_2 -> Tri-ROO·		1.1x10^6	sec.$^{-1}$ (pseudo-first order)	[6,7]
R9	2 Tri-ROO· -> 2 RC=O + ROH		4.0x10^{-15}	cm^3 molec.$^{-1}$ sec.$^{-1}$	[6]
R10	2 Tri-ROO· -> 2 Tri-RO· + O_2		1x10^{-16}	cm^3 molec.$^{-1}$ sec.$^{-1}$	[6]
R11	RO· + RH -> R· + ROH		1.66x10^{-15}	cm^3 molec.$^{-1}$ sec.$^{-1}$	[6]
R12	·OH + Tri -> Tri-OH·		6.60x10^{-11}	cm^3 molec.$^{-1}$ sec.$^{-1}$	[8]
R8b	Tri-OH· + O_2 -> β-ROO·		1.1x10^6	sec.$^{-1}$ (pseudo-first order)	[6,7]
R9b	2 β-ROO· -> 2 RC=O + ROH		4.0x10^{-15}	cm^3 molec.$^{-1}$ sec.$^{-1}$	[6]
R13	β-ROO· -> CI + ROH		120	sec.$^{-1}$	[9]
R14a	C9_aldehyde (bulk) => C9_aldehyde_des		1x10^4	sec.$^{-1}$	*
R14b	C9_aldehyde_des => C9_aldehyde (g)		4.12x10^5	sec.$^{-1}$	**

Ozonolysis reaction mechanism adapted from Zeng & Wilson.[9]

* Estimated diffusion time across a 200 nm distance with a diffusion coefficient corresponding to that of Tri (D ≅ 7.15x10^{-7} cm^2 sec.$^{-1}$)

** Estimated from nonanal vapor pressure (~0.3 torr at 25 ˚C) according to the method described in the Supporting Information of Heine, et. al.[2]

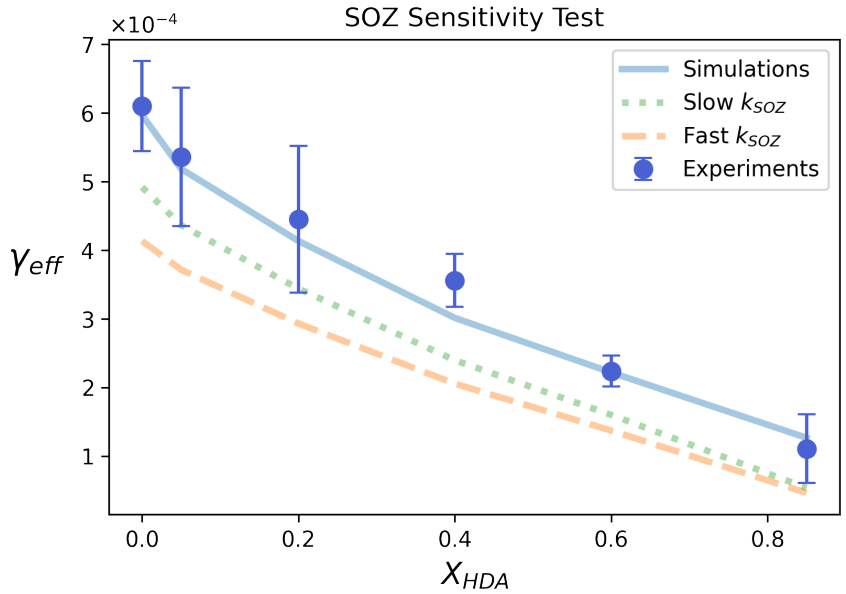

Figure S5A: Effective uptake coefficients predicted by stochastic model, with sensitivity tests of SOZ formation pathway involving C14 aldehyde species. Two rate constants k_{SOZ} for reaction R6 were used: the rate coefficient used in stochastic kinetic simulations reported by Heine et. al[2] (denoted "Slow k_{SOZ}," 1.3×10^{-18} cm^3 $molec.^{-1}$ $sec.^{-1}$) and the rate reported used in flux-based simulations as reported by Müller et al.[10] (denoted "Fast k_{SOZ}," 10^{-15} cm^3 $molec.^{-1}$ $sec.^{-1}$).

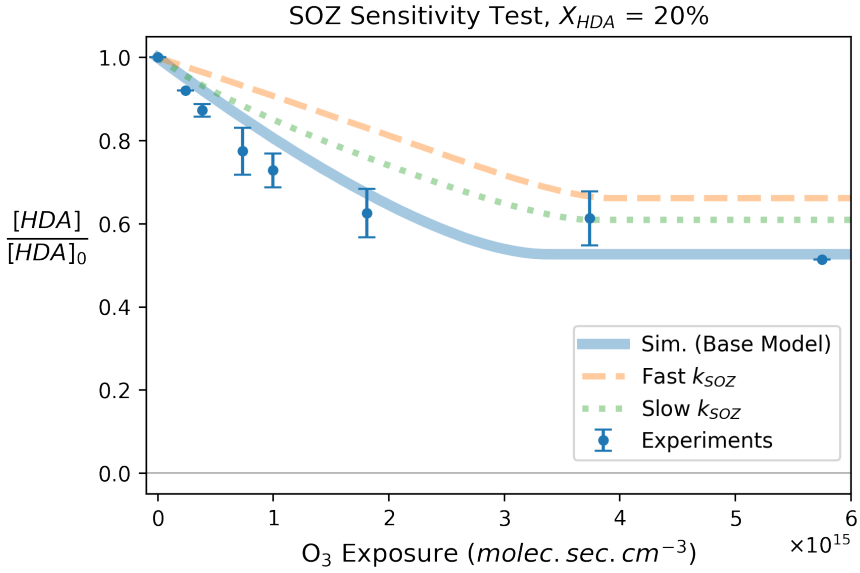

Figure S5B: Simulated decay traces of HDA for 20% mole fraction HDA conditions, under the base model (Scenario A from main text, with no SOZ formation pathway) and SOZ formation sensitivity test scenarios described in S5A above.

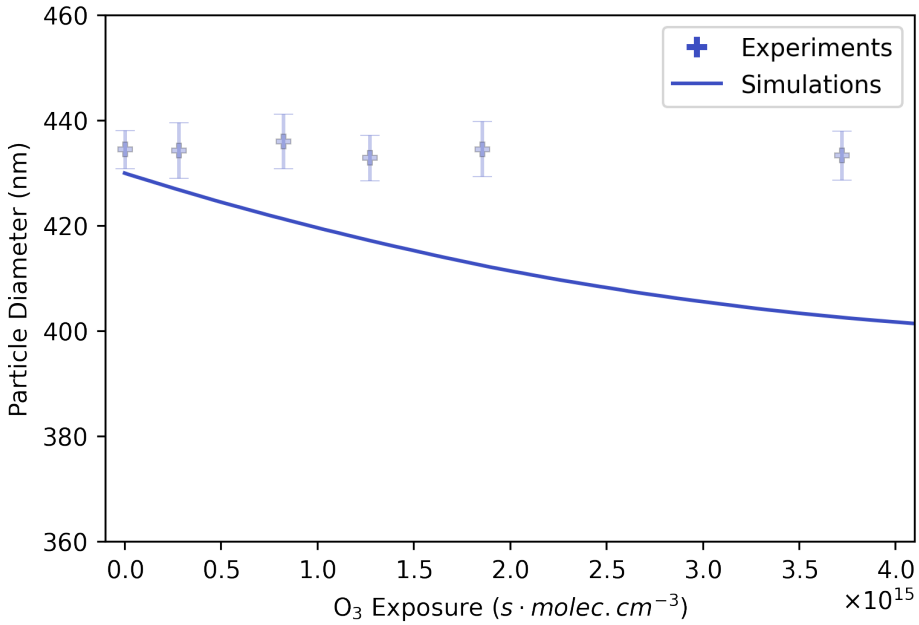

Figure S6A: Diameter changes observed in experiments (points, error bars are ±1σ of three measurements) and those predicted by explicit kinetic simulation (solid lines) accounting for the evaporation of nonanal from neat Tri aerosol during ozonolysis.

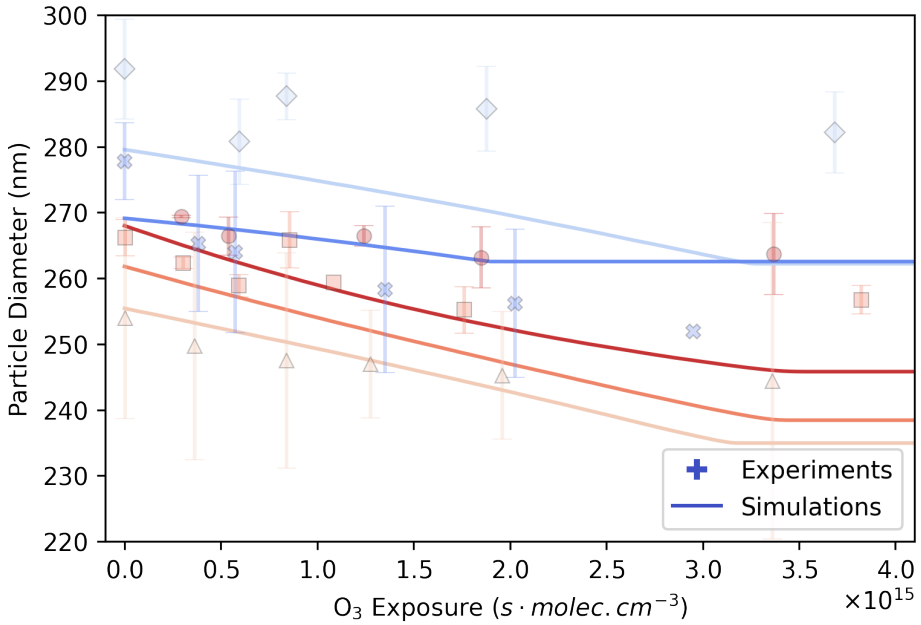

Figure S6B: Diameter changes observed in experiments (points, error bars are ±1σ of at least three measurements) and those predicted by explicit kinetic simulation (solid lines) accounting for the evaporation of nonanal from aerosol binary mixtures of Tri/HDA having the mole fractions described in Table S1.

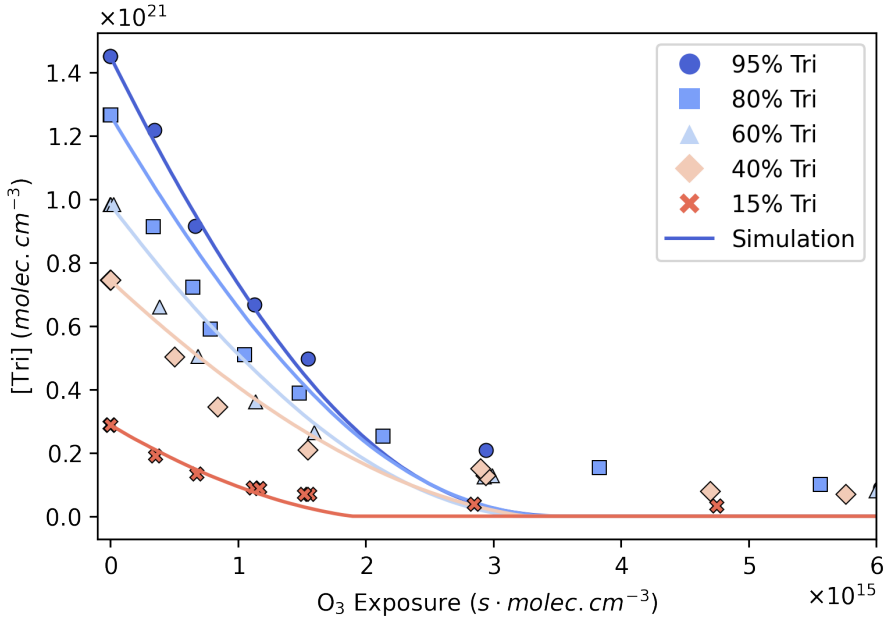

Figure S7: Decay kinetics of Tri at each HDA mole fraction, comparing experimental observations (points) and explicit kinetic simulations under modeling Scenario A (solid lines), where k_{AAHP} = 2.2x10^{-19} cm^3 molec.$^{-1}$ sec.$^{-1}$

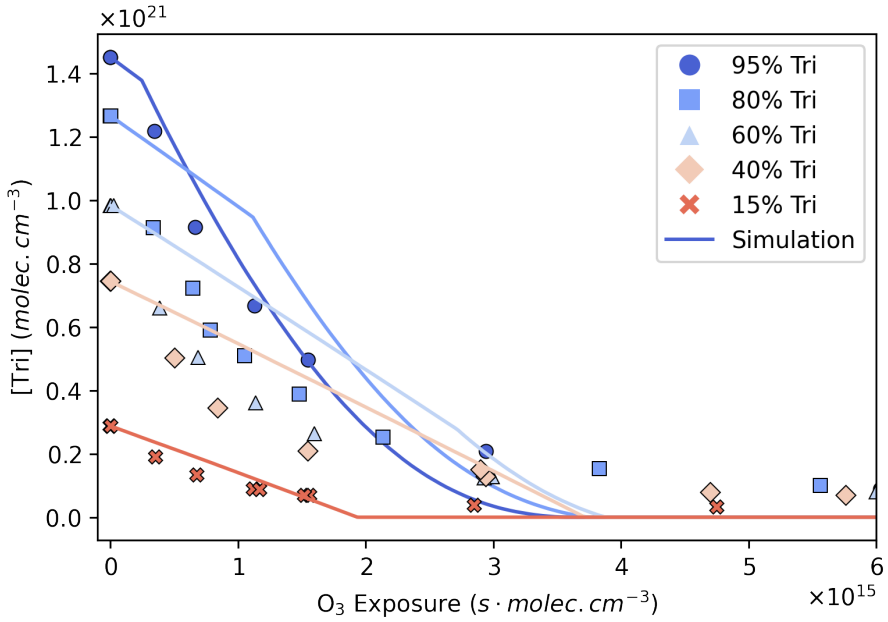

Figure S8: Decay kinetics of Tri at each HDA mole fraction, comparing experimental observations (points) and explicit kinetic simulations under modeling Scenario B (solid lines). In Scenario B, k_{AAHP} is set to 1x10^{-13} cm^3 molec.$^{-1}$ sec.$^{-1}$ representing the diffusion limit in an organic matrix.

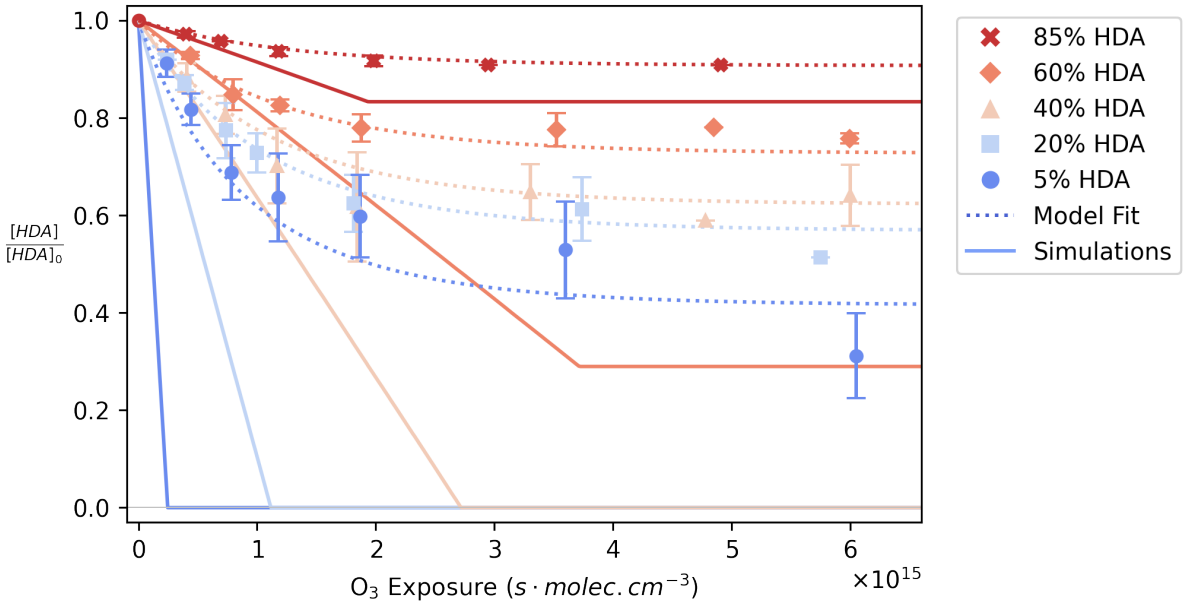

Figure S9: The decay of the HDA signal intensity with ozone exposure, normalized to unreacted HDA signal for aerosols having HDA mole fractions (from top to bottom) of 85%, 60%, 40%, 20%, and 5%. Solid lines represent the results of explicit kinetic simulations under Scenario B, where k_{AAHP} = $1x10^{-13}$ cm^3 $molec.^{-1}$ $sec.^{-1}$, as described in Section 4.3 of the main text.

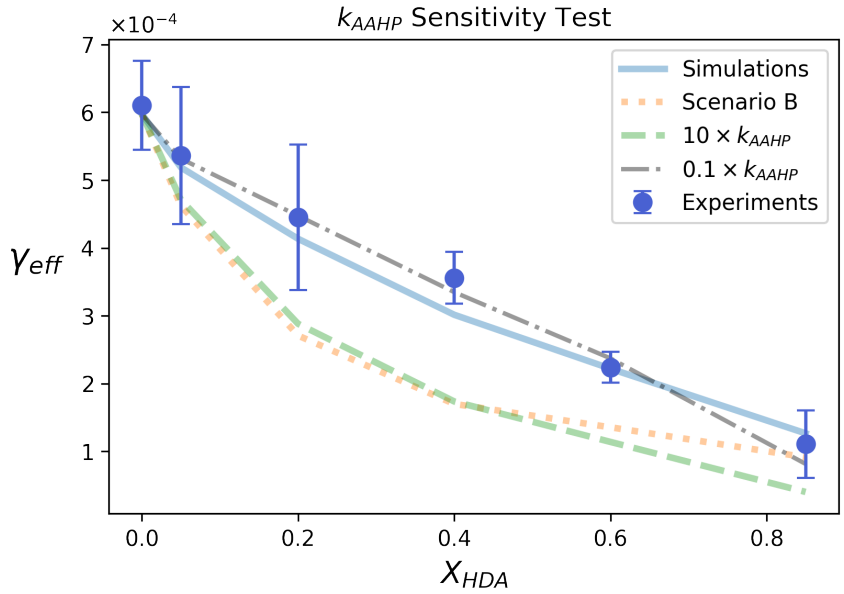

Figure S10A: Effective uptake coefficients (γ_{eff}) predicted by the stochastic kinetic model under different modeling assumptions: Scenario A (base model, labeled "Simulations") and Scenario B as described in the main text, and values of k_{AAHP} one order of magnitude faster (10 x k_{AAHP}) and slower (0.1 x k_{AAHP}) than the optimal value adopted in the base model.

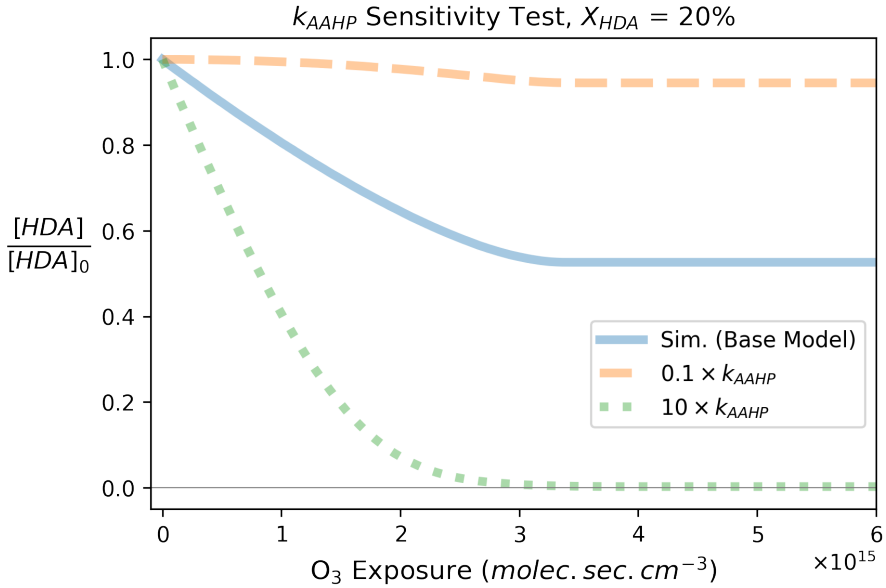

Figure S10B: Decay traces of HDA for 20% mole fraction HDA conditions, under the base model (Scenario A from main text) and ±1 order of magnitude rate k_{AAHP} rate constants as described above, illustrating the sensitivity of the predicted HDA kinetics to the specification of k_{AAHP} in the model.

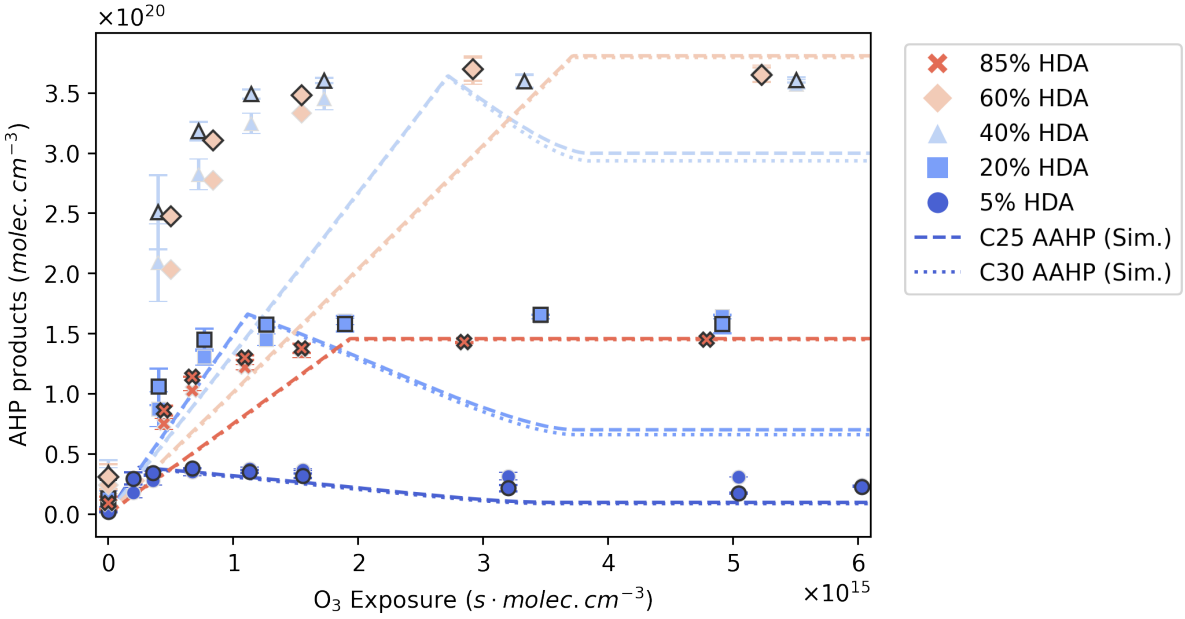

Figure S11: The kinetic evolution of AAHP reaction products at each HDA mole fraction, comparing experimental observations (points) to the results of explicit kinetic simulations under Scenario B (solid lines). Observations correspond to integrated intensities of mass spectral peaks corresponding to AAHP products. Light-outlined points correspond to C25 AAHPs (m/z = 397 in positive ion mode and m/z = 669 in negative ion mode), and dark-outlined points correspond to C30 AAHPs (m/z = 467 in positive ion mode and m/z = 739 in negative ion mode); see Section 3.1. Experimental data is scaled to match the maximum product concentration of each simulation result.

References:

(1) Roveretto, M.; Li, M.; Hayeck, N.; Brüggemann, M.; Emmelin, C.; Perrier, S.; George, C. Real-Time Detection of Gas-Phase Organohalogens from Aqueous Photochemistry Using Orbitrap Mass Spectrometry. *ACS Earth Space Chem.* **2019**, *3* (3), 329–334. https://doi.org/10.1021/acsearthspacechem.8b00209.

(2) Heine, N.; Houle, F. A.; Wilson, K. R. Connecting the Elementary Reaction Pathways of Criegee Intermediates to the Chemical Erosion of Squalene Interfaces during Ozonolysis. *Environ. Sci. Technol.* **2017**, *51* (23), 13740–13748. https://doi.org/10.1021/acs.est.7b04197.

(3) Vereecken, L.; Novelli, A.; Taraborrelli, D. Unimolecular Decay Strongly Limits the Atmospheric Impact of Criegee Intermediates. *Phys. Chem. Chem. Phys.* **2017**, *19* (47), 31599–31612. https://doi.org/10.1039/C7CP05541B.

(4) Vereecken, L.; Peeters, J. H-Atom Abstraction by OH-Radicals from (Biogenic) (Poly)Alkenes: C–H Bond Strengths and Abstraction Rates. *Chemical Physics Letters* **2001**, *333* (1), 162–168. https://doi.org/10.1016/S0009-2614(00)01347-6.

(5) Atkinson, R. Estimations of OH Radical Rate Constants from H-Atom Abstraction from C–H and O–H Bonds over the Temperature Range 250-1000 K. *International Journal of Chemical Kinetics* **1986**, *18* (5), 555–568. https://doi.org/10.1002/kin.550180506.

(6) Denisov, E. T.; Afanas'ev, I. B. *Oxidation and Antioxidants in Organic Chemistry and Biology.*; Taylor & Frances: Oxford, 2005.

(7) Houle, F. A.; Hinsberg, W. D.; Wilson, K. R. Oxidation of a Model Alkane Aerosol by OH Radical: The Emergent Nature of Reactive Uptake. *Phys. Chem. Chem. Phys.* **2015**, *17* (6), 4412–4423. https://doi.org/10.1039/C4CP05093B.

(8) Peeters, J.; Boullart, W.; Pultau, V.; Vandenberk, S.; Vereecken, L. Structure−Activity Relationship for the Addition of OH to (Poly)Alkenes: Site-Specific and Total Rate Constants. *J. Phys. Chem. A* **2007**, *111* (9), 1618–1631. https://doi.org/10.1021/jp066973o.

(9) Zeng, M.; Wilson, K. R. Efficient Coupling of Reaction Pathways of Criegee Intermediates and Free Radicals in the Heterogeneous Ozonolysis of Alkenes. *J. Phys. Chem. Lett.* **2020**, *11* (16), 6580–6585. https://doi.org/10.1021/acs.jpclett.0c01823.

(10) Müller, M.; Mishra, A.; Berkemeier, T.; Hausammann, E.; Peter, T.; Krieger, U. K. Electrodynamic Balance–Mass Spectrometry Reveals Impact of Oxidant Concentration on Product Composition in the Ozonolysis of Oleic Acid. *Phys. Chem. Chem. Phys.* **2022**, *24* (44), 27086–27104. https://doi.org/10.1039/D2CP03289A.